THESIS FOR THE DEGREE OF DOCTOR OF PHILOSOPHY

Transient *In Situ* Studies on Supported Catalysts

CO_2 Methanation and Methane Oxidation

Felix Hemmingsson

CHALMERS

Department of Chemistry and Chemical Engineering
CHALMERS UNIVERSITY OF TECHNOLOGY
Göteborg, Sweden 2021

Transient *In Situ* Studies on Supported Catalysts

CO_2 Methanation and Methane Oxidation

Felix Hemmingsson

ISBN 978-91-7905-460-1

Doktorsavhandlingar vid Chalmers tekniska högskola

Ny serie Nr. 4927

ISSN 0346-718X

Department of Chemistry and Chemical Engineering
Chalmers University of Technology
SE-412 96 Göteborg
Telephone +46 31 772 1000

Cover:
An illustration of a potential closed loop cycle of a methanation process, for which energy is inserted to the system by H_2, O_2 and CH_4 formation, and later released by combustion of CH_4.

Typeset in LaTeX using the kaobook class

Printed by Chalmers Digitaltryck

Göteborg, Sweden 2021

Transient *In Situ* Studies on Supported Catalysts
CO_2 Methanation and Methane Oxidation
Felix Hemmingsson
Department of Chemistry and Chemical Engineering
Chalmers University of Technology

Abstract

This dissertation aims to increase the understanding of important steps in the catalytic CO_2 hydrogenation and total methane oxidation reactions over supported noble metal catalysts. A general theme is the role of the metal oxide support for the catalytic reactions. In the case of methane oxidation, the reported detrimental effect of water is of primary interest.

A range of powder catalysts were prepared by incipient wetness impregnation including Rh/MO (MO = SiO_2, Al_2O_3, CeO_2) and Pd/MO (MO = Al_2O_3 and ZSM-5) for CO_2 hydrogenation and methane oxidation, respectively. The catalysts were studied *in situ* using high-energy X-ray diffraction, ambient pressure X-ray photoelectron spectroscopy and X-ray absorption spectroscopy as to follow structural dynamics and with diffuse reflectance infrared Fourier transform spectroscopy to monitor surface species. Transient measurements were designed and obtained data were analysed with phase sensitive detection in order to distinguish inactive (spectator) species from active ones.

For CO_2 hydrogenation on the rhodium catalysts, an initial step of dissociation of carbon dioxide into carbon monoxide (and oxygen) occurs on the rhodium phase, and is enabled by the presence of hydrogen. The irreducible supports (SiO_2 and Al_2O_3) show a minor contribution to the catalytic mechanism whereas for the CeO_2 based catalysts, several kinds of carbonyls (b-CO, h-CO, m-CO) and carbonates (b-CO_3, p-CO_3) are active species. While more experimental data is needed as to establish the complete pathway, the activity of the carbonyl species suggests that the reaction follows a carbon monoxide based pathway such as the carbide route.

As for the detrimental effect of water on the methane oxidation, two aspects are shown to be of critical importance. The first concerns the build up of a low but strongly inhibiting hydroxyl coverage on the PdO nanoparticles hampering their redox dynamics and seemingly shifting the operating mechanism from a Mars-van Krevelen to a Langmuir-Hinshelwood type of mechanism that proceeds slower. The second is the support hydrophilicity, which contributes to inhibition of important active sites on the rim of the developed PdO nanoparticles through the formation of surface hydroxyls.

The knowledge about the catalyst structure-function relationships obtained in this work may be used to guide future catalyst design and synthesis, and catalyst operation, as to provide more efficient catalytic processes.

Keywords: Sabatier reaction; CO_2 reduction; CH_4 oxidation; Catalytic methanation; Hydrogenation; *In situ* spectroscopy; HE-XRD; AP-XPS; DRIFTS; XAS; Heterogeneous catalysis

List of Publications

This thesis is based on the following appended papers:

I. Structure–function relationship during CO_2 methanation over Rh/Al_2O_3 and Rh/SiO_2 catalysts under atmospheric pressure conditions

N. M. Martin, F. Hemmingsson, X. Wang, L. R. Merte, U. Hejral, J. Gustafson, M. Skoglundh, D. M. Meira, A.-C. Dippel, O. Gutowski, M. Bauer and P.-A. Carlsson

Catalysis Science & Technology, 8 **(2018)**, *2686-2696*

II. Structure-function relationship for CO_2 methanation over ceria supported Rh and Ni catalysts at atmospheric pressure conditions

N. M. Martin, F. Hemmingsson, A. Schaefer, M. Ek, L. R. Merte, U. Hejral, J. Gustafson, M. Skoglundh, A.-C. Dippel, O. Gutowski, M. Bauer, and P.-A. Carlsson

Catalysis Science & Technology, 9 **(2019)**, *1644-1653*

III. CO_2 methanation over Rh/CeO_2 studied with infrared modulation excitation spectroscopy and phase sensitive detection

F. Hemmingsson, A. Schaefer, M. Skoglundh and P.-A Carlsson

Catalysts, 10 **(2020)**, 601

IV. Hampered palladium oxide redox dynamics by water decreases the activity for total methane oxidation

P. Velin, F. Hemmingsson, A. Schaefer, M. Skoglundh, K. A. Lomachenko, A. Raj, D. Thompsett, G. Smedler and P.-A. Carlsson

Submitted

V. The role of surface carbonyls and carbonates in the catalytic CO_2 hydrogenation over ceria supported rhodium and nickel

F. Hemmingsson, A. Schaefer, M. Skoglundh and P.-A Carlsson

In manuscript

My Contributions to the Publications

Paper I

I participated in the planning of and carrying out the HE-XRD measurements and data reduction as well as setting up the experimental equipment. I also partook in the XAS measurements, followed the data analysis of the HE-XRD and XAS studies and co-authored the paper.

Paper II

I participated in the planning of and carrying out the HE-XRD measurements and data reduction as well as setting up the experimental equipment. I also followed the data analysis of the HE-XRD study and co-authored the paper.

Paper III

I prepared the sample, designed and performed all experiments and analyses, excluding XRF. In addition to this, I also designed and assembled the equipment set-up and wrote the software for the gas system. I wrote the first draft of the manuscript and was responsible for the writing process and to respond to the reviewers' comments.

Paper IV

I participated in the XAS measurements, and in the analysis of XAS and IR data. I participated in the design and structure of figures and, in the writing of the manuscript.

Paper V

I designed and performed all experiments and analyses, excluding XRF, and wrote the first draft of the manuscript.

Publications not included in the thesis:

Methane Adsorption and Methanol Desorption of Copper Modified Boron Silicate

X. Wang, A. Shishkin, F. Hemmingsson, M. Skoglundh, F. J. Martinez-Casado, L. Bock, A. Idström, L. Nordstierna, H. Härelind and P.-A. Carlsson

*RSC Advances, 8 (***2018***), 3639-36374*

Acknowledgements

This research was funded by the Knut and Alice Wallenberg foundation through the project "Atomistic design of Catalysts" (No. 2015.0058) and the Swedish Research Council through the Röntgen-Ångström collaboration “Synergistic development of X-ray techniques and applicable thin oxides for sustainable chemistry” (No. 2017-06709).

Competence Centre for Catalysis, which is hosted by Chalmers University of Technology and financially supported by the Swedish Energy Agency and the member companies: AB Volvo, ECAPS AB, Johnson Matthey AB, Preem AB, Scania CV AB, Umicore AG & Co. KG and Volvo Car Corporation AB

Parts of the work have also been performed at the synchrotron research facilities PETRA III (DESY), Advanced Light Source (ALS) and European Synchrotron Radiation Facility (ESRF). The provision of beamtime as well as assistance from beamline scientists is gratefully acknowledged. Additionally, parts of this work have been performed at Chalmers Materials Analysis Laboratory (CMAL).

I would also like to thank:

My main supervisor Per-Anders Carlsson and examiner Magnus Skoglundh for giving me this opportunity and all your help and guidance throughout these years. Thank you for always sparing a moment to help out even when you yourselves have been overloaded. All your input has been invaluable.

My collaborators, in particular Andreas, Natalia and Peter for all your work, help and tutelage. I would surely have been wandering in the dark without you.

Lennart Norberg, Lasse Urholm and Ulf Stenman, without their help in setting up equipment this work would have ground into a halt at quite an early stage.

Hanna Härelind, Anders Palmqvist, Carina Jogevik, Frida Andersson and Lotta Pettersson for the often overlooked but oh so important administrative work and for organising parties and other fun activities through these years.

All my current and previous friends and colleagues at TYK and KCK, of which there are simply too many to list here, but as it is said, you know who you are. I would like to thank Adam, Alvaro, Anne, Carl-Robert, Christopher, Colin, David, Ida, Johanna, Leo, Linfeng, Mats, Simone and Xueting especially for all your help and stimulating discussions.

Finally, my family for all their love support all throughout my life.

Felix Hemmingsson, Göteborg, March 2021

Contents

List of Figures

List of Tables

Abbreviations, acronyms and terms

ν_y(X)	Symmetric (y = s) or asymmetric (y = a) stretching of group X, see page 16
δ(X)	Symmetric in-plane bending, scissoring, of group X, see page 16
ω(X)	Symmetric out-of-plane bending, wagging, of group X, see page 16
m-X	X complexed in a monodentate fashion
b-X	X complexed in a bidentate fashion to one site
br-X	X complexed in a bidentate fashion to two sites (bridged)
p-X	X complexed in a multidentate fashion with multiple sites (polydentate)
γ	Dispersion, see page 9
λ	Wavelength
ϕ_k^{PSD}	The operator controlled phase angle/phase angle for demodulation for the k^{th} harmonic frequency, see page 11
τ	Time period
$\tilde{\nu}$	Wavenumber, reciprocal wavelength
φ_k	Phase delay in regards to the k^{th} harmonic frequency, see page 11
A	Absorbance *or* area
$A_k^{\phi_k^{PSD}}$	The phase-resolved amplitudal data for a given operator controlled angle and harmonic frequency, see page 11
d	Interplanar distance in a crystal structure, see page 13, *or*, diameter
F_{tot}	Total flow, in this work given as milliliter normal (0 °C, 1 bar) per minute
q	Scattering vector, see page 13
R	Reflectance, see page 16
y_i	Partial gas composition in regards to substance i. Expressed as molar or volumetric percent of the gas that is constituted by i
AP-XPS	Ambient pressure X-ray photoelectron spectroscopy, see page 14
BET	Brunauer-Emmett-Teller, adsorption, see page 8
DRIFTS	Diffuse reflectance infrared Fourier transform spectroscopy, see page 16
ED-XAS	Energy dispersive X-ray absorption, see page 14

EXAFS	Extended X-ray absorption fine structure, see page 14
HE-XRD	High energy X-ray diffraction, see page 13
IR	Infrared, see page 16
MES	Modulation excitation spectroscopy, see page 10
PSD	Phase sensitive detection, see page 11
TEM	Transmission electron microscopy, not explained in this thesis
TOF	Turn over frequency, see sidenote at page 37
WLI	White line intensity, see page 14
XANES	X-ray near-edge structure, see page 14
XAS	X-ray absorption, see page 14
XPS	X-ray photoelectron spectroscopy, see page 14
XRD	X-ray diffraction, see page 13
XRF	X-ray fluorescence, see page 15

Introduction 1

1.1 The question of fuel

The search for sustainable energy sources and systems has amassed a significant interest among societal actors, engineers and researchers. While the focus often, and perhaps foremost, has been on the availability of energy sources, an important shift towards questions regarding energy storage and fuels that are not sourced from fossil reserves has been witnessed during the latest decades.[1,2] Though energy harvesting by wind and solar power shows great promise as "green" energy solutions,[3] their dependence on external factors, e.g., weather, season and grid load, make them lack the necessary on-demand energy supply capability.[4] This currently limits their possibility of constituting a larger portion of countries' energy system if not an energy buffer can be introduced. One such buffer could be the formation of gaseous hydrogen (H_2) by for instance water splitting (equation (1.1)). Thereby the obtained energy is chemically stored in the hydrogen bond. This concept could be set up as a closed system by recycling the constituent molecules and is thus characterised by a zero net consumption/production of H_2O/H_2.[5]

Indeed, the concept of using H_2 as a basal energy vector has by itself gained much attention and the concept has been coined the *hydrogen economy*.[6] Even if H_2 is easily cycled and suitable applied in electrical systems, by the use of fuel cells,[7] there are still a number of inherent problems associated with the broader use of H_2. For combustion systems, for example, a low H_2 concentration in the gas stream is tolerable[1] but higher concentrations poses safety risks in terms of corrosion, i.e., hydrogen embrittlement, with consequential risk of leakage.[9–11] Furthermore, due to it being a gas at normal conditions, which is relevant for the majority applications, H_2 lacks the appropriate energy density and has a high storage cost in comparison to other fuels.[12] In order to circumvent these problems, it is possible to convert H_2 into alkanes and alcohols by hydrogenation of carbon oxides, i.e., carbon monoxide (CO) and carbon dioxide (CO_2).[2] In contrast to H_2, long-chained alkanes and alcohols are liquids at normal conditions and can often be applied directly[2] in existing systems such as combustion engines. However, while obtaining high energy densities and low storage costs, the processes for the production of these fuels incur an energy loss and require expensive high-pressure chemical reactor systems. Further, while being suitable for long-term storage and clearly usable for automotive applications,[13,14] the role of long-chained alkanes and alcohols for short-term energy cycling is questionable.

$$2\,H_2O \rightleftharpoons 2\,H_2 + O_2 \qquad (1.1)$$

1: Furthermore, for certain applications an addition of hydrogen could prove beneficial, such as the case of utilisation of hydromethane (natural gas and hydrogen mixtures).[8]

2: Or with minor adjustments.[13] Furthermore, as these are base chemicals they are also of interest for applications other than fuel.

1.2 Catalysis for energy applications

$$CO_2 + 4\,H_2 \longrightarrow CH_4 + 2\,H_2O \quad (1.2)$$

The Sabatier reaction (equation (1.2)) was originally developed for removal of carbon oxides from hydrogen streams but has gained renewed interest in recent times thanks to the methane (CH_4) product that is an attractive energy carrier.[3][12]

3: In addition, some niche applications have arisen, such as the removal of CO_2 from air and recycling of H_2O, as done at the international space station.[15]

Although CH_4 has lower energy density compared to long-chain alkanes and alcohols, its ease of production makes it suitable for intermediate storage times and short-term energy cycling.[16] Furthermore, it can be utilised in current technologies developed for natural gas in regards to transport and usage, thus decreasing the implementation cost. However, when used as fuel, it is important to abate methane emissions as the CH_4 molecule is a strong greenhouse gas.[4][18] The common approach is to add on catalytic exhaust aftertreatment technologies for total oxidation of methane. Despite the fact that a chemical reaction might be energetically favoured, that alone may not warrant it being plausible. Take as an example diamonds. While De Beers slogan is *a diamond is forever*[19] they are in fact unstable[20] and degrade slowly forming graphite.[5] Fortunately, the degradation time amounts to billions of years[6] because the degradation reaction is (strongly) kinetically limited, i.e., the reaction rate is sluggish, which is a characteristic that many industrially relevant reactions share. To speed up the kinetics one may, for example, heat up the sample because the rate of chemical reactions increases with increased temperature. The downside with heating is that it will not only increase the running cost of the reaction but might also open up for unwanted side reactions lowering the desired reaction selectivity. A fascinating approach to circumvent this problem is the usage of a catalyst. While the catalyst can not change the free energy of a reaction, i.e. a thermodynamically impossible reaction remains impossible, it can greatly increase its rate towards equilibrium by providing an alternative reaction pathway.[21] Analogously, one can envision the catalytic process as taking a shortcut. We still move from point A to B[7] but use less energy intense steps to do so. A more formal description is depicted in Figure 1.1. Here E_a is the activation energy of the reaction, the energy needed for the reaction to occur, and I_x are the intermediary steps of the reaction. Like the shortcut, a catalyst is not consumed by its use. However, its shape and behaviour may change during the reaction cycle, but returns to the state of the initial step after completing the reaction cycle.[21]

4: Indeed, having a global warming potential (GWP) 28-36 times greater than CO_2.[17]

5: Diamond → Graphite [20]
$\Delta G_f^\circ = -2.9\,\mathrm{kJ\,mol^{-1}}$

6: And as such you do not need to worry about your engagement ring slowly turning into a decorative, and impractical, pencil during your lifetime.

7: i.e., the change in potential energy remains unchanged

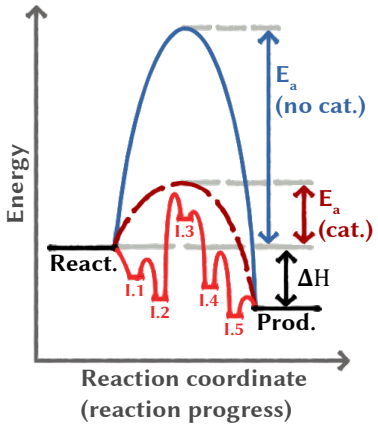

Figure 1.1: Schematic energy diagram for a reaction, showing the activation energy (E_a) for a non-catalysed reaction and a catalysed reaction. For the catalysed reaction, an apparent change in activation energy is shown as the dashed line whereas the full line shows the actual reaction with intermediary steps. As such, the barriers seen between the intermediary steps represent the activation energy for each individual reaction step.

1.3 Motivation of this work

The slow kinetics of catalysts for the Sabatier reaction makes high temperatures and pressures needed in order to gain industrially relevant yields.[22,23] As such, the development of catalysts capable of operating close to ambient conditions would decrease the energy intensity of the process and open up for the methanation reaction to be run in less expensive industrial units and/or smaller remote apparatuses. Once methane is produced and used as fuel, the emission of methane from the combustion system must be strictly controlled. As such, limiting factors of this reaction must be determined and finally resolved or reduced.

Background 2

In this work, while the formation of methane by carbon dioxide hydrogenation (Sabatier reaction, Section 2.1) using rhodium based catalysts has been the main focus, the consumption of methane by oxidation has also been studied in regards to its sensitivity to water vapour (Section 2.2). However, both these studies have been focused on the reaction mechanisms of these catalysts by relating the activity with the material structural change and surface adsorbates.

2.1 The Sabatier reaction

During the turn of the 20th century, Paul Sabatier together with Jean-Baptiste Senderens discovered what is now known as the Sabatier reaction, shown in equation (2.1), for which Sabatier was awarded the Nobel prize in chemistry in 1912.[24] While originally utilised for purification of gaseous hydrogen from carbon oxides, it has now gained a renewed interest due to applications such as fuel production, energy storage and oxygen recycling.[12]

$$\begin{aligned} \mathrm{CO_2(g) + 4\,H_2(g) \longrightarrow CH_4(g) + 2\,H_2O(g)} \\ \Delta H_{298\,\mathrm{K}} = -165\,\mathrm{kJ\,mol^{-1}} \end{aligned} \tag{2.1}$$

The reaction is strongly exothermic and the drop in entropy limits the maximum conversion of the Sabatier reaction at atmospheric pressure, unless carried out at low temperatures. As such, industrially elevated temperature and pressure is utilised in order to achieve fast kinetics and to avoid the limitation to the maximum conversion.[22,23] In regards to energy usage[1] and simplicity of equipment, a low temperature and pressure solution might be more suitable. Operating at atmospheric conditions, initial activity at temperatures as low as 200 °C and operable temperatures (high conversion) as low as 300 °C are not uncommon for methanation catalysts.[25,26]

1: In addition to general industrial production, for some applications such as the previously noted air purification at the international space station,[12] more complex systems such as those employing elevated pressures might be unsuited.

Ever since the days of Sabatier, methanation catalysts are predominantly composed of nickel, most often deposited on high surface metal oxide supports.[12,23,27] While metals such as rhodium and ruthenium can surpass nickel in regards to activity, the high activity and selectivity together with much lower price makes nickel based catalysts so far more favourable.[23,26] However, some aspects limit the nickel catalysts such as deactivation by oxidation and formation of volatile carbonyls at low temperatures (< 300 °C), and carbon deposition.[12,22,23,28,29] For these reasons, noble metals are still of interest in the pursuit of decreased reaction temperature for CO_2 methanation.

Proposed reaction mechanisms

While a black box approach of catalyst screening allows for the discovery of new well performing catalysts using also some chemical intuition, it can seldom provide the insight needed to finely tune the properties of the catalyst[2]. In order to accomplish this, knowledge of the reaction mechanism is needed in order to, for example, determine the rate determining step of the reaction and the cause behind its limitation. For CO_2 methanation, as well as CO_2 hydrogenation in general, the reaction pathway is commonly following one of three different routes: the formate, carbon monoxide[3]and carboxylate pathway.[12] Among these, it is the carbon monoxide and formate routes that have been observed experimentally, see equations (2.2)-(2.8).[12,27] For the traditional Ni catalysts, *e.g.*, Ni/SiO_2, Ni/Al_2O_3 and the like, which have enjoyed an extensive amount of studies, the carbide pathway[4] in which the CO dissociates and forms elementary carbon (C) that is further hydrogenated into CH_4 is the most commonly attributed pathway.[12,23,27] However, while proceeding by a carbon monoxide based pathway, the intermediary steps of the nickel based catalysts have been shown to be dependent on the support. As an example, an IR study of a Ni/ZrO_2 catalyst where the ZrO_2 is an active support, intermediary bicarbonates and formates were observed, see equations (2.24)-(2.26).[27] As such, while studying the reaction mechanism one may encounter an interplay between pathways as well as red herrings as the observation of intermediates most commonly associated to certain pathways might lead to the conclusion that the reaction follows that particular pathway.

2: One property that is often tuned, by example choice of support, promoter and active material, is the adsorption strength of the reactants towards the catalyst. According to Sabatier's principle, adsorbates may not adsorb too strongly, as they then will not desorb, nor too weakly, as not enough accumulations of adsorbates occur and the adsorption is too weak for dissociation.[21]

3: Also called the reverse water-gas shift (rWGS) or carbide pathway, based on pre- and succeeding steps.

4: Reaction steps of the carbide pathway.[27]

$$CO_2 + H_2 + * \rightarrow CO^* + H_2O \quad (2.2)$$
$$CO^* + H_2 \rightarrow C^* + H_2O \quad (2.3)$$
$$H_2 + 2\,^* \rightarrow 2\,H^* \quad (2.4)$$
$$C^* + H^* \rightarrow CH^* + * \quad (2.5)$$
$$CH^* + H^* \rightarrow CH_2{}^* + * \quad (2.6)$$
$$CH_2{}^* + H^* \rightarrow CH_3{}^* + * \quad (2.7)$$
$$CH_3{}^* + H^* \rightarrow CH_4 + 2* \quad (2.8)$$

$*$: Empty adsorption site
i^* : Adsorbed i

Reaction steps of the formate pathway as shown in the review by Vogt et al.[12]

$$H_2 + 2\,^* \rightarrow 2\,H^* \quad (2.9)$$
$$CO_2 + H^* \rightarrow HCOO^* \quad (2.10)$$
$$HCOO^* + 2\,H^* \rightarrow HCO^* + H_2O \quad (2.11)$$
$$HCO^* + H^* \rightarrow H_2CO^* + * \quad (2.12)$$
$$H_2CO^* + H^* \rightarrow H_2COH^* \quad (2.13)$$
$$H_2COH^* + H^* \rightarrow CH_2{}^* + * \quad (2.14)$$
$$CH_2{}^* + H^* \rightarrow CH_3{}^* + * \quad (2.15)$$
$$CH_3{}^* + H^* \rightarrow CH_4 + 2* \quad (2.16)$$

However, as this pathway may involve a metal oxide, several additional potential reaction steps can be imagined such as the formation of a methoxy group (CH_3O^-). This would then be similar to proposed formate pathways for other hydrogenation catalysts, such as those for CO_2 into methanol.[30] If so, by tuning the characteristics of the catalyst one could open the possibility of producing other products.

One could also envision non-CO or formate based pathways, such as the following one studied by Ren et al. for the Ni(111) surface[31]:

$$H_2 + 2* \rightarrow 2\,H^* \quad (2.17)$$
$$CO_2 + * \rightarrow CO_2{}^* \quad (2.18)$$
$$CO_2{}^* + 2\,H^* \rightarrow C(OH)_2{}^* + 2* \quad (2.19)$$
$$C(OH)_2{}^* + H^* \rightarrow CH_2O^* + OH^* \quad (2.20)$$
$$CH_2O^* + H^* \rightarrow CH_2{}^* + * \quad (2.21)$$
$$CH_2{}^* + H^* \rightarrow CH_3{}^* + * \quad (2.22)$$
$$CH_3{}^* + H^* \rightarrow CH_4 + 2* \quad (2.23)$$

$$CO_2 + OH^{-,*} \longrightarrow HCO_3{}^{-,*} \quad (2.24)$$
$$HCO_3{}^{-,*} + H_2 \longrightarrow HCOO^{-,*} + H_2O \quad (2.25)$$
$$HCOO^{-,*} + * \rightleftharpoons CO^* + OH^{-,*} \quad (2.26)$$

2.2 Methane oxidation

Due to the methane molecule being nonpolar, structurally symmetric and highly stable, its interaction with catalyst surfaces is generally weak such that a near complete methane conversion by oxidation can be quite a challenge to achieve.[32] Indeed, this is greatly seen during exhaust gas treatment, as although only a low concentration of methane remains, a high content of inhibiting water (10-15 vol.%) is present.[33] This requires elevated temperatures not only in order to drive the methane oxidation itself forward, but also to prohibit a significant formation of water adsorbates on the catalyst. Indeed many studies have been devoted to understand the active phase[34,35] and the role of the support[36,37] under dry conditions and fewer studies have been reported for the corresponding wet conditions.[38,39] Also a large focus has been on stability of the catalyst as the exhaust temperatures reach as high as 800-900 °C.[40] However, with an increased fuel efficiency the exhaust gas temperature have in turn decreased as well, which further complicates the removal of methane.[40] As such, the focus towards these catalysts have shifted towards low temperature oxidation catalysts. Of these, palladium

based catalysts have received considerable attention due to their high activity, perhaps in particular Pd/γ-Al_2O_3 due to its high activity and the stability of the Al_2O_3 support.[41–43]

Water inhibition

While these palladium based catalysts display enviable characteristics in a dry feed, they suffer greatly from water inhibition as well as water induced sintering at higher temperatures (creating a permanent deactivation).[33] While being generally accepted that the reaction follows a Mars-van Krevelen mechanism (see Figure 2.1), no clear understanding regarding how water inhibits the reaction has been obtained although formation of an inactive $Pd(OH)_2$ phase and/or blockage of surface PdO by hydroxyl adsorbates have been proposed.[44–46] Of these, the formation of $Pd(OH)_2$ may be questioned due to its low stability at the reaction temperatures.

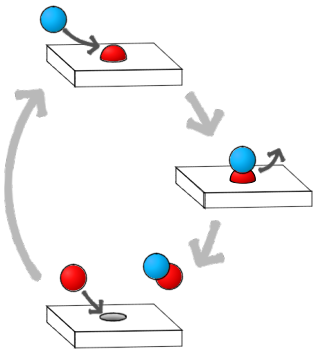

Figure 2.1: A cartoon illustrating the Mars-Van Krevelen reaction model. Note that unlike the Langmuir-Hinshelwood model which is displayed in Figure 2.2, the surface atom of the first step is part of the facet and not simply adsorbed to the surface. As such, a hole is left which must be refilled.

2.3 Using transient *in situ* studies to reveal reaction mechanisms

While both *ex situ* and *in situ* studies in regards to the surface reactions are often conducted with ease by the use of methods such as infrared spectroscopy (see Section 3.5), the behaviour of the catalyst material during the reaction is not as easily studied, often leaving it as an *ex situ* comparison of the fresh and spent material. Crucial information such as the restructuring of the catalyst during the reaction may therefore go unnoticed. Furthermore, not only active species but also spectators, a species that is formed at reaction conditions but does not participate in the (main) reaction,[47] may be observed and falsely attributed as a true main reaction intermediate. Additional factors must therefore be included as to separate the contributions of active and spectators species, for which transient studies are common. This is further discussed in some depth in Section 3.3.

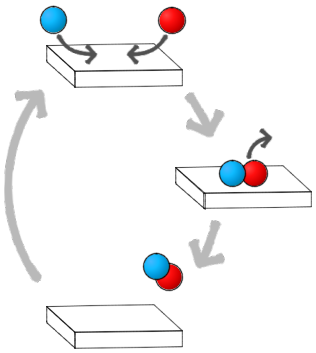

Figure 2.2: A cartoon illustrating the Langmuir-Hinshelwood reaction model. In this model, the reactants first adsorb to the surface, undergo reaction and the formed product then desorbs.

2.4 Objectives of the studies

The theme of this thesis is to elucidate the role of the support material for CO_2 methanation and methane oxidation over supported noble metal catalysts. Specifically, it aims at providing fundamental understanding of the behaviour of Rh/MO (MO = Al_2O_3, SiO_2 and CeO_2) methanation catalysts under operation conditions and a first insight into the mechanistic pathway of the CO_2 methanation reaction over this type of catalyst. Furthermore, some of the involved mechanisms for inhibition by water on the methane oxidation and its relation to choice of support is presented by a study of two types of palladium catalysts, Pd/Al_2O_3 and Pd/ZSM-5 (SAR = 5000), a hydrophilic and hydrophobic support, respectively.

Methodology 3

In this work, the *in situ* behaviour of the catalyst material and the surface reactions over the catalyst for the considered chemical reaction were studied. To accomplish this, the changes in crystal structure and oxidation state was studied using synchrotron X-ray sources (Section 3.4) and the adsorbates of the reaction was studied by infrared spectroscopy (Section 3.5). As both active, those that participate in the reaction, and spectators, those that do not participate in the reaction, are observed in the resulting data, these experiments were conducted transiently using a modulation excitation approach (Section 3.3) in order to remove the contribution of spectators from the data set.

3.1 Catalyst preparation

In order to achieve a highly efficient heterogeneous (solid) catalyst, it must exhibit a high specific surface area (m^2/g) on which the active sites are located as to optimize its effective volume. In the case of supported catalysts, the supporting material must be able to carry and stabilise the active particles.[21,48] Production methods of these catalysts, range from top-down approaches, such as milling the active material into a very fine powder, to bottom-up approaches in which, for example, well defined nanoparticles may be synthesised and later deposited on a support.[49–52] Another bottom-up approach is the formation of the particles on the support material directly, via impregnation with a precursor material.[50] This simple route is a commonly used synthesis route, not only due to its simplicity but also ability to create well dispersed nanoparticles on a support.[50] While being the easiest to imagine, impregnation using excess solvent and thermally drying produces unsatisfactory results, as effects such as drag forces from the liquid results in pore blockage and large size dispersion of the particles, lowering the material utilization. As such, an alternative method is the incipient wetness impregnation, in which the amount of solvent is limited to the volume needed to fill the pores of the support. Furthermore, in order to dry the sample while immobilising the precursor, the impregnated sample is then frozen and dried under vacuum.[50] These impregnation methods are conceptually illustrated in Figure 3.1.

In this thesis, the alumina, silica and ceria supported rhodium catalysts were prepared by incipient wetness impregnation, using $Rh(NO_3)_3$ (Paper I and II), and Rh dissolved in nitric acid (Paper III and V) as metal precursors. The palladium samples of the oxidation study (Paper IV) were prepared using both nitrate and non-nitrate precursors. The pore volume was estimated by the addition of the solvent to a reference support sample, marking the volume as the last point before any liquid film could be detected.

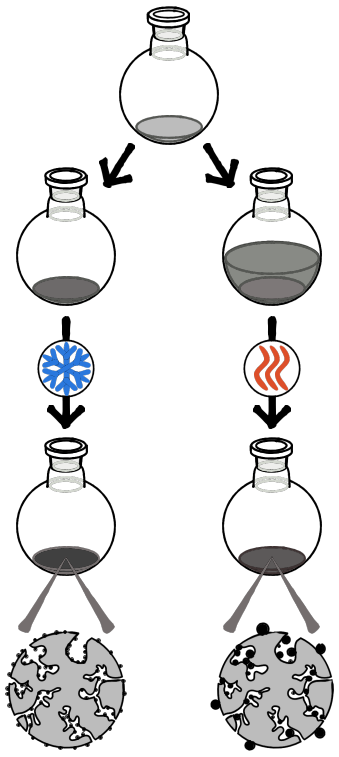

Figure 3.1: Illustration showing the start and end state of impregnation performed as dry impregnation (left) and one with excess of solvent and thermally dried (right). For the thermally dried sample, the formation of large particles, localised at pore openings and clogging pore channels may occur.

3.2 Surface characterisation by gas adsorption

For adsorption, the material doesn't enter the bulk of the other material (absorption) but instead adheres to the surface of it, either as individual molecules/atoms or it forms a film on the surface. Due to this, the adsorption and adherence of a fluid to a solid may reveal several structural properties, such as surface area, pore size and its distribution as well as surface composition. In this work, the specific surface surface area (SSA) has been measured by physisorption and the size and dispersion of the active metal have been probed by chemisorption.

Surface area: Brunauer-Emmett-Teller (BET) theory

A commonly used method to quantify the specific surface area (SSA) of a porous material is that of gas sorption. The SSA (S) of a material can be calculated by equation (3.1) in which the surface area is related to the area occupied by the adsorbed gas. Obtaining V_m is typically done by BET[1] theory. The concept of this theory is that an inert gas, typically N_2, is adsorbed to the surface in a layer-by-layer fashion and by finding the volume of one layer it is possible to calculate the surface area.[53] This model has a number of assumptions[2] which for a real system might not hold true, especially for microporous materials. However, it provides an sufficiently accurate estimation. The BET equation is given below in equation (3.2), for which P_0 is the vapour pressure, V is the volume of adsorbed gas and c is the BET constant.

$$S = \frac{V_m \sigma N_A}{m V_0} \tag{3.1}$$

V_m : Volume of a monolayer
σ : Surface area of an adsorbate
N_A : The Avogadro constant
m : Mass of the porous material
V_0 : Molar volume of the gas

1: An acronym of the researchers who proposed the theory: Stephen **B**runauer, Paul Hugh **E**mmett and Edward **T**eller

2: BET theory assumes the following:[21]

- Adsorption and desorption rate are equal, at any layer
- Adsorption sites at layer 1 are equivalent
- For layer N≥2
  - All adsorption sites are equivalent
  - The adsorption energy is equal to the condensation energy
  - The N^{th} layer acts as adsorption sites for the N+1 layer
- No adsorbate-adsorbate interaction
- Only one adsorbate per adsorption site
- As $P \rightarrow P_0$, multilayer thickness $\rightarrow \infty$

$$\frac{P}{V(P_0 - P)} = \frac{c-1}{V_m c}\left(\frac{P}{P_0}\right) + \frac{1}{V_m c} \tag{3.2}$$

One may obtain V_m from (3.2) by applying it to an adsorption isotherm data set together with a regression, resulting in V_m being equal to 1/(Gradient + y-Intercept).

In this work, the BET model has been put into practice in order to measure the SSA of the samples. A general approach in the measurements has been an initial drying step at elevated temperatures (e.g. 250 °C) for 1-2 h, followed by drying at lower temperature (e.g. 100 °C) for a longer time period, ~12 h, while flowing N_2 in order to remove adsorbed water. Nitrogen isotherms were afterwards collected at -196 °C using a Micromeritics Tristar 3000 instrument.

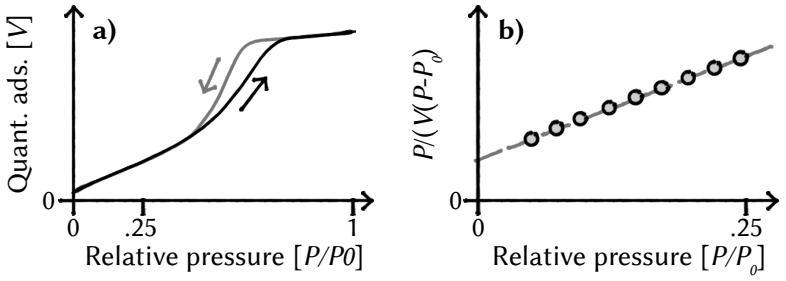

Figure 3.2: Drawing of an adsorption-desorption isotherm for a mesoporous material (a) and a BET plot for the isotherm.

Selective probing by adsorption: Chemisorption

In contrast to physisorption, a chemisorbed substance forms a chemical bond to the surface. As such, the adhesion of a chemisorbed substance greatly surpasses that of a physisorbed one. Furthermore, given that the support of a material does not adsorb a gas while the deposited particle do, one can separate the surface area of the deposited particle from that of the total surface. Analogous to the specific surface area, the surface area of this particle can be obtained by measuring the volumetric uptake of the probe molecule, as shown in equation (3.3). However, unlike that of the BET method the mode of adsorption of this probe molecule onto the surface must be taken into regard as a molecule may adsorb on one or more sites and as such a stoichiometric factor F_S must be included.[54]

The dispersion (γ) of a deposited material, i.e. the fraction of the material which is exposed to the surface, can be calculated by the use of chemisorption, as shown in equation (3.4), by a simple relation to the number of adsorbates and how many sites they occupy compared to the amount of the metal. Likewise, by adding an expression for the shape of the particle, its average size can be estimated by equation (3.5).

The steps of a typical chemisorption experiment are illustrated in Figure 3.3. In order to remove contaminants and form the site of interest, a number of pre-treatments (PT) may be performed at elevated temperatures, which might require a gas treatment during cooling (C) to be stabilised. After this preparation, the sample undergoes two cycles of vacuum drying and adsorption. During the first cycle both the chemisorption and physisorption occurs and after this, one treats the sample with vacuum, thereby depleting the surface of physisorbed species. As such, only physisorption occurs during the second cycle and thus the difference between these two cycles corresponds to the amount of chemisorbed gas. An additional step, which is not illustrated, of the pre-treatment could also be the adsorption of a poison, whose role it is to block certain sites as to exclude them in the adsorption measurement.

In this work, CO chemisorption has been used in order to determine the dispersion, mean particle size and metal surface area of the deposited Pd particles of the Pd/Al_2O_3 and Pd/ZSM-5 samples. The pre-treatment consisted of 5 vol.% O_2 followed by 5 vol.% H_2 at 550 °C and then cooling the sample to 35 °C in a flow of H_2. After this, the adsorption isotherms were recorded using a Micromeritics ASAP 2020. This procedure was later repeated in an infrared study[3] in order to obtain the F_s parameter.

$$A_i = n_a F_S a_s N_A \tag{3.3}$$

$$\gamma_i = \frac{V_{\text{Chem.}} M_i F_S}{V_{\text{mol}} w_i} \tag{3.4}$$

$$d_i = \frac{\kappa}{A_{i,s} \gamma \rho} \tag{3.5}$$

A_i : Surface area of i
n_a : Mole of adsorbate
F_s : Adsorption sites per adsorbate
a_s : Adsorbates cross-section area
N_A : The Avogadro constant
γ_i : Dispersion of i
$V_{\text{Chem.}}$: Vol. of chemisorbed adsorbate at the monolayer per mass i
M_i : Molar mass of i
V_{mol} : Molar volume of adsorbate
w_i : Mass fraction of i in the sample
d_i : Mean diameter of i
κ : Particle surface area to volume ratio divided by its diameter†
$A_{i,s}$: SSA of i, A_i/m_i

†: For spheres (and its partitions), κ in equation 3.5 is equal to 6 $[(\pi\, d^2)/(\pi\, d^3/6) = 6/d]$

3: Infrared spectroscopy is introduced in Section 3.5.

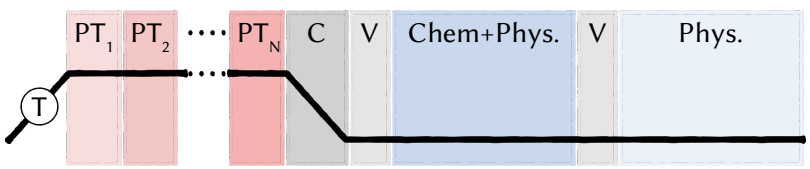

Figure 3.3: The typical steps of a chemisorption measurement, consisting of a number of pre-treatments with oxidation and/or reduction treatments at elevated temperatures followed by a cool-down with or without a stabilising gas. After the pre-treatment, two adsorption isotherms are collected with intermittent vacuum drying steps.

3.3 Separating active species from spectators by modulation excitation

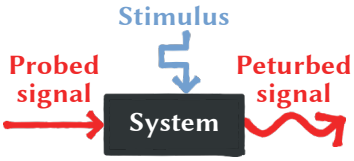

Figure 3.4: A conceptual sketch of an MES experiment. Behaviour and content of the system which otherwise would be hidden can be determined indirectly by studying its response to a stimulating signal.

Establishing the reaction pathway based on steady-state measurements can be quite a daunting task, as distinguishing true intermediates from spectators may be night impossible. As such, experiments for this task are favourably conducted transiently, of which the *modulation excitation* experimental model is a common approach. The fundamental idea of this method is that by periodically disturbing the system, parameters which are dependent on the stimulus[4] will in turn show a periodic response, whereas spectators that are not dependent on the stimulus typically exhibit an initial response and later may reach a steady-state.[55] The simplest example of how this perturbation could be achieved in heterogeneous catalysis is to switch on and off the feed of one of the reactants. The expected response is thus a shift in the coverage on the catalyst as the consumption and production rates of the individual adsorbates are shifted. Furthermore, by changing the modulant[5] the system's dependence on different parameters can be obtained. Another critical parameter is the modulation frequency, as a too low frequency would let slow side-processes, such as accumulation of spectators, to exhibit a response whereas a too high frequency may instead produce a too low response from the system and thus be hard to detect.

Given that the system produces a repeatable response from the stimulus, the response from a large number of pulses may be performed, accumulated and averaged in order to not only produce data of a high time resolution but a high signal-to-noise as well.

As an example, consider the hypothetical reaction $A + B_2 \longrightarrow E$ that is heterogeneously catalysed (solid catalyst, gaseous reactants). This reaction is composed of the intermediary steps given through equation (3.6) to (3.10). In addition to this, spectators are formed by a rapid and slow side reaction, equation (3.11) and (3.12) respectively. Keeping the example simple, this model assumes no mass transport limitations, all the reactions occur on an extended flat surface and all adsorbate species except A′ are adsorbed on the same type of adsorption site, and the system is isothermal. By modulating the partial pressure of A (p_A) in the form of a sinus function while the partial pressure of B (p_B) remains constant, a response similar to the one shown in Figure 3.5 may be obtained. As expected, all reaction intermediates respond to this stimulus, albeit weakly for some, and the slow side reaction (3.12), while initially responding, reaches a steady-state[6] due to its slow kinetics. These slow responses can be expected from highly stable, non-interactive, species such as carbonate and hydroxides. However, while this slow spectator could be filtered out by modulation excitation spectroscopy (MES) approach, the spectator with a rapid reaction, (3.11), still shows a response. A relevant example to this work would be the equilibrium reaction $HCOO \rightleftharpoons CO + OH$.

4: e.g. the dependence the coverage of adsorbates on a particle has on the gas concentration of a reactant.

5: The parameter which is periodically changed, be it gas concentration, temperature, pressure, voltage, etc., any parameter which may control the reaction could theoretically be used.

Reaction steps of the simulated reaction

$$A + * \rightleftharpoons A^* \tag{3.6}$$
$$B_2 + 2* \rightleftharpoons 2\,B^* \tag{3.7}$$
$$A^* + B^* \rightleftharpoons C^* + * \tag{3.8}$$
$$C^* + B^* \rightleftharpoons E^* + * \tag{3.9}$$
$$E^* \longrightarrow E + * \tag{3.10}$$
$$A^* + B^* \rightleftharpoons D^* + * \tag{3.11}$$
$$A^* \rightleftharpoons A'^* \tag{3.12}$$

$*$: Empty adsorption site
i^* : Adsorbed i

$$\theta_i = \frac{\text{Nr of sites occupied by } i}{\text{Total number of sites}} \tag{3.13}$$

6: Or what appears to be a steady-state, in actuality it still shows a response, it is simply too weak to detect.

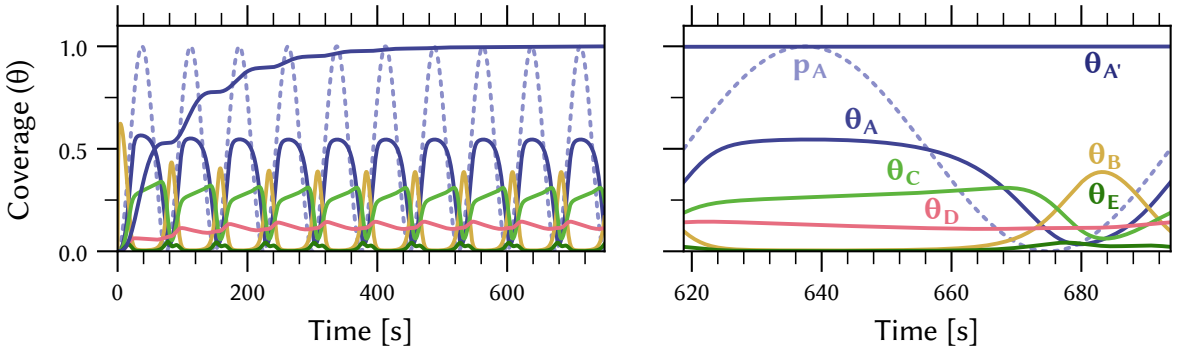

Figure 3.5: Simulated ME experiment in which a primary reaction is sinusoidally modulated. In the left figure, the reaction initiation followed by multiple modulation steps are shown. A single period after the system has reached a constant oscillation is shown in the right.

Phase-sensitive detection

For data obtained from modulation excitation measurements, removal of the static signal and extraction of the delay for the responding signal compared to the modulation is a main target. In order to accomplish this, so-called phase sensitive detection (PSD) can be applied, either by Fourier transform or, as in this study, by a lock-in amplifier, expressed in regards to a transient IR data set in equation (3.14).[56] In equation (3.14), the $A(\tilde{\nu}, t)$ term is the amplitude in the time-domain, $k\omega$[7] is the analysed frequency, τ is the period time, ϕ_k^{PSD} is the so called operator controlled phase angle and $A^{\phi^{\mathrm{PSD}}}$ is the phase-resolved amplitudal data.[57]

$$A_k^{\phi^{\mathrm{PSD}}}(\tilde{\nu}) = \frac{2}{\tau}\int_0^{\tau} A(\tilde{\nu}, t)\sin\left(k\omega t + \phi_k^{\mathrm{PSD}}\right)\mathrm{d}t \tag{3.14}$$

By applying equation (3.14) to MES data, signals that do not show a periodic response to the stimulus, such as noise and spectators, are reduced or fully cancelled out and integration over additional periods further increases the signal-to-noise ratio.[57] As an example, by solving this on the previous simulated MES example (Figure 3.5) for the full phase period ($0° \leq \phi_k^{\mathrm{PSD}} \leq 360°$) with the same frequency as the p_{A} modulation results in Figure 3.6.

By finding the phase delay φ_k, i.e. how much out-of-phase the response is to the stimulus, one may sequence the order of events in a data set of multiple responses.[58] This phase delay can be obtained from the in-phase ($\phi_k^{\mathrm{PSD}} = 0°$) and out-of-phase ($\phi_k^{\mathrm{PSD}} = 90°$) amplitudes, as shown in (3.15) and (3.16).[56] Solving the phase delays for the simulated example, one obtains a $|\varphi_k|$ order of D<A<C<E<B, providing the correct reaction sequence (A ⟶ C ⟶ E).

As a square wave function may be expressed as a sum of infinite odd numbered harmonics (equation (3.18), Figure 3.8) one may study several frequencies[8] from a single square wave MES experiment, given the corrections shown in equation (3.19) and (3.20).[58] In practice, the MES-PSD experiment and analysis encounter instrumental limitations and complications. A minor problem for example is the broadening of the square wave due to diffusion. While actuating a well defined square wave by the use of fast-switches and pressure stabilisation, this shape will not remain due to diffusion broadening as the gas travels in the gas line. However, in this work the largest limiting factor to the study is

7: For which $k = 1$ corresponds to the fundamental vibration, $k = 2$ is the first harmonic, $k = 3$ the second harmonic and so on.

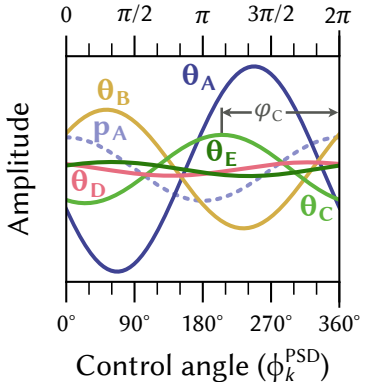

Figure 3.6: The phase resolved data of the simulated MES experiment, shown in Figure 3.5, solved for $k = 1$.

$$A_k(\tilde{\nu}) = \sqrt{A_k^{0°}(\tilde{\nu})^2 + A_k^{90°}(\tilde{\nu})^2} \tag{3.15}$$

$$\cos\varphi_k = \frac{A_k^{0°}(\tilde{\nu})}{A_k} \tag{3.16}$$

$$\sin\varphi_k = \frac{A_k^{90°}(\tilde{\nu})}{A_k} \tag{3.17}$$

$$x(t) = \frac{4}{\pi}\sum_{n=1}^{\infty}\frac{\sin[(2n-1)\omega t]}{2n-1} \tag{3.18}$$

$$A_{2n-1}^{SW} = \frac{4A^{\sin}|_{\omega'=(2n-1)\omega}}{\pi(2n-1)} \tag{3.19}$$

$$\varphi_{2n-1}^{SW} = \varphi^{\sin}|_{\omega'=(2n-1)\omega} \tag{3.20}$$

8: Note that the Nyquist-Shannon theorem still limits the highest studiable frequency to half the sampling frequency.

the sample cell[9] that contains a significant dead volume. As such, the square wave suffers from large deformation, which can be seen for the case of τ =120 s CO_2 modulation[10] in Figure 3.7. Furthermore, higher modulation frequencies in this cell also disallows a full purge of the modulated gas and a minimum is instead introduced. However, even with these problems, one can still study the fundamental frequency of the pulse and perturbation of the system, albeit with an included error function.

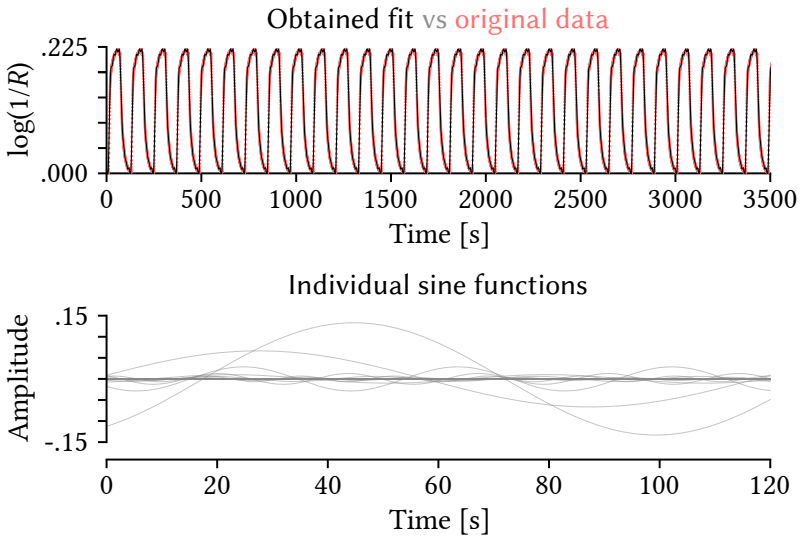

Figure 3.7: Frequency composition, illustrated as sine functions, of the pulse shape corresponding to τ = 120 s, solved for the first 43 frequencies of the data set, calculated by discrete Fourier Transform using the fast Fourier transform (FFT) algorithm. The graph at the top is the fitted data and resulting function. Beneath, the individual sine functions of the fitted sum of sine. Note that the period lengths of the individual sine functions do not follow a multiple of the fundamental frequency (as was the case for the square wave).

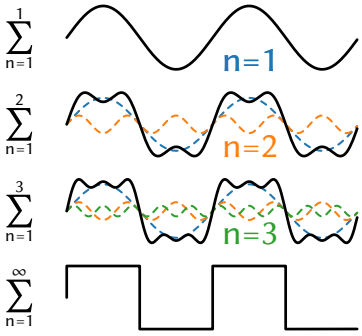

Figure 3.8: An illustration of how a square wave is constructed by the use of an infinite number of sinusoidal functions.

How MES has been applied in this work

The MES approach has been widely used in this work, including the study of changes in crystal structure, oxidation state and formation and consumption of surface species.[11] It is foremost the latter in which it's contribution has had the greatest weight, being complemented with phase-sensitive detection in order to study the reaction intermediates. Applying MES allowed for the removal of spectator signals from the IR characterisation of adsorbates during *in situ* CO_2 methanation over Rh/CeO_2. Furthermore, by analysing phase delays, some proposals for reaction mechanisms are given.

9: The high temperature reaction chamber for the Praying Mantis™ cell, shown in Section 3.5.

10: The displayed pulses were obtained with F_{tot} = 125 ml_n min^{-1}, 1 vol.% CO_2. While this was the flow in paper V, in paper III F_{tot} was instead 200 ml_n min^{-1} which reduced the impact of gas dispersion, resulting in the formation of a more square-like pulse shape. However, the F_{tot} = 125 ml_n min^{-1} case is shown here to highlight how much the modulation that the sample experiences can deviate from what was fed.

11: Methods which will be presented at page 13, 14, 14 and 16 respectively.

3.4 Obtaining catalyst structure and composition by X-ray radiation

The high energy of X-ray photons, and consequently their short wavelength, allows one to study the crystalline structure of long range order of the material down to Ångström scale (diffraction) as well as to characterise the oxidation state and composition of a material by probing its core electrons (X-ray absorption, X-raf photoelectron spectroscopy and X-ray fluorescence). All these methods suffer from the limitations of conventional laboratory X-ray equipment in the form of a lack of high energy and photon flux (also referred to as brilliance) as well as a tunable X-ray source, which is limiting what can be observed as well as prohibiting transient studies. As such, for applications such as studies of a catalyst behaviour one typically perform these experiments at synchrotrons.

Crystal structure: X-ray diffraction

Made famous by Young's double slit experiment, the bending of light is an optical phenomenon that occurs if it passes through slits with a size similar to or less than its wavelength. This diffraction can, as shown by Von Laue, be used to determine the crystal structure of a material, due to its planes of atoms forming a near-infinite number of repeating slits.[59,60] As typical inter-atomic distances are in the Ångström scale, high energy radiation such as X-rays are needed to provide the suitable wavelength for the experiment. After the pioneering work of Von Laue, a simpler description was later provided by Bragg, relating the the diffraction angle (θ) with the inter-planar distance (d) and wavelength (λ).[61] This relation is known as Bragg's law and can be seen in equation (3.21) and a schematic representation of the process can be seen in Figure 3.9.[60] While the diffraction caused by a perfect single crystal, which has a defined orientation, results in discrete and clear diffraction spots, randomly oriented samples such as powders produce ring patterns.[60] Nevertheless, the diffraction angle is still the same.

The obtained diffraction data is typically presented as a diffractogram, i.e., the measured intensity of the diffracted X-rays against its corresponding diffraction angle as 2θ. As the angle of diffraction in equation (3.21) is wavelength dependent, direct comparison of diffractograms produced by X-rays of different wavelengths is prohibited. By re-expressing it as a wavelength independent constant this problem can be circumvented. One may to accomplish this by moving from the ℝ-space expression to that of the k-space and the usage of the Laue equations,[12] expressing it as a relation between the diffraction angle and wavelength, see equation (3.23). Furthermore, the expression of q_{hkl}will only be dependent on the lattice spacing, d, making it instrumentally independent, see equation (3.22).

In this study, the rhodium based catalysts were studied by high energy X-ray diffraction (HE-XRD) with a high photon flux supplied by synchrotron radiation at the P07 beamline at PETRA III (Deutsches Elektronen-Synchrotron, DESY) using an in house fabricated *in situ* cell.[64] The high energy and photon flux allowed for a detailed transient *in situ* study, which is prohibited by conventional lab X-ray sources.

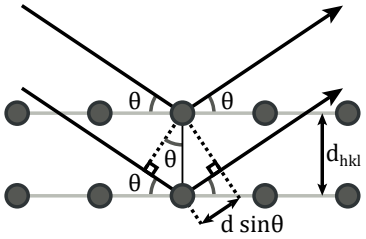

Figure 3.9: Schematic representation of Bragg's law. Individual atoms are shown as balls and lines highlighting the crystal plane have been added. Note that the two shown scattered photons share angle and will constructively interfere, providing a defined maximum intensity. Furthermore, the extra distance for the lower photon gives rise to the $2d\sin(\theta)$ in Bragg's law.

$$2d\sin(\theta) = n\lambda \tag{3.21}$$

d : Interplanar distance
θ : Diffraction angle
n : A positive integer
λ : Wavelength of the refracted light

12: The k-space, a metonym for the reciprocal space, is visualisation of the Fourier transform of the ℝ-space expression. The basic concept is to express the Bravais lattice in regards to its periodicity, and then visualise these vector sets as wave vectors. From this, one may realise that the incident and reflected light ($\mathbf{k}_0$ and $\mathbf{k}$ respectively) will have a moduli of $2\pi/\lambda$ and only show a constructive interference at $q_{hkl} = \boldsymbol{k} - \boldsymbol{k}_0$, for which q_{hkl} is the scattering vector. Based on this, equation (3.22) can be defined and its relation to Bragg's law can be established as equation (3.23).[62,63]

$$q_{hkl} = \frac{2\pi}{d} \tag{3.22}$$

$$q = \frac{4\pi}{\lambda}\sin(\theta) \tag{3.23}$$

d : Interplanar distance
q : Scattering vector
λ : Wavelength of the refracted light
θ : Diffraction angle

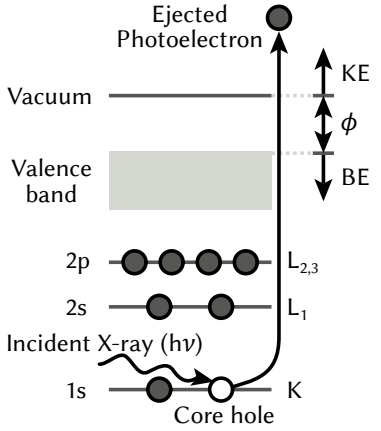

Figure 3.10: A schematic figure showing the ejection of a photoelectron from the 1s orbital of oxygen by an X-ray photon. KE refers to the kinetic energy whereas BE is the binding energy. ϕ is the work function of the instrument.

Surface state: X-ray photoelectron spectroscopy

The discovery of the photoelectric effect, i.e., the emission of (most commonly) an electron following the absorption of electromagnetic radiation, have lead to numerous different applications out of which X-ray photoelectron spectroscopy is important in the field of catalysis research.[21,65] The process involves the ejection of a core electron from an atom by the absorption of highly energetic photons, X-rays. By measuring the kinetic energy of this ejected photoelectron one can find the original binding energy of said electron by equation (3.24), given that the energy of the X-ray photon ($h\nu$) and work function of the instrument (ϕ) are known.[21] This process is illustrated in Figure 3.10. An atoms electron is not an island, interaction within the atoms electron cloud as well as neighbouring atoms will shift the energy of this core electron. As such, this binding energy not only reveals the kind of atoms present in the sample, but also provides an insight into their oxidation state and local environment by studying the so called chemical shift.

As the photoelectron need to be able to escape the material without being reabsorbed, the probing depth of this technique only extends to a few nanometers, making it a surface sensitive technique. However, this consequently often limits XPS to pressures $\leq 10^{-6}$ mbar due limitations to the path length of the emitted photoelectron by inelastic scattering by the surrounding gas phase.[66] As such, *in situ* studies by XPS have been severely limited in regards to catalysis studies. In more recent years, ambient pressure XPS (AP-XPS) in which the gas pressure around the sample is close to reactant/product partial pressures relevant in many applications has become possible thanks to sophisticated instrumental setup and high photon flux, supplied by synchrotron sources.[66–68]

In this study, the oxidation state of the Rh/CeO_2 catalyst as well as the formation of some adsorbates formed was studied during CO_2 methanation by the use of AP-XPS at the beamline 9.3.2 at ALS (Advanced Light Source), Berkeley USA.

$$E_{\text{binding}} = h\nu - E_{\text{kinetic}} + \phi \qquad (3.24)$$

h : Planck's constant
ν : Frequency of the incident photon
ϕ : The work function of the instrument

Oxidation state: X-ray absorption spectroscopy

As it names suggests, in X-ray absorption spectroscopy (XAS) it is the absorption of the incoming X-ray radiation by the material which is used as the analytical tool. Like the case of XPS, the core electrons of the atom may absorb the incoming X-ray radiation of a certain energy and enter an excited state. However, unlike XPS it is not ejected photoelectrons which is of interest but rather the amount of incoming radiation that is absorbed and what energy the photons of said radiation carried[13]and how the electrons are scattered. As such, XAS do not suffer the limitations of XPS such as the need for a vacuum and a conductive sample.[69] However, the probed volume of the sample is changed, from primarily the surface with a few nanometers depth, which is the case of XPS, to potentially probing the full volume of the sample, as is the case of XAS.[21,69,70] In regards to quantification for XAS, the spectrum of a transmission XAS can be constructed and quantified by the use of the Beer-Lambert law for each individual energy, equation (3.25). Lacking the absorption coefficient, one can simply perform the quantification of, for example, the oxidation by linear combination.[14][69,70]

$$A = \mu x = \log \frac{I_0}{I_T} \qquad (3.25)$$

μ : Linear absorption coefficient
x : Sample thickness
I_0 : Intensity of incident photon
I_T : Intensity of transmitted photon

13: Using either a monochromator, single wavelength, or polychromator, a spectrum, using diffraction, see Section 3.4. For the polychromator, the incident wavelengths are separated by angles and the individual wavelengths can thus be recorded by sampling different angles of the transmitted radiation. This setup with polychromator is referred to as Energy-Dispersive XAS (ED-XAS).[69]

14: For example, by an interpolation between standard samples.

Due to the information and shape of the resulting spectrum from XAS, one refers to it as the X-ray absorption fine structure (XAFS), schematically showed in Figure 3.11. This structure consists of two regions, the X-ray absorption near-edge structure (XANES) which is located around the absorption edge, the sharp absorption increase, and the higher energy level following XANES is the extended X-ray absorption fine structure (EXAFS). The EXAFS region contains inter-atomic interactions of the scattered electrons which forms the observed interference pattern.[69,70] As such, one may extract information regarding the local structure of the material, such as inter-atomic distances, from this region by the use of Fourier transform.[69] In the XANES region, it is the absorption edge that is of interest as it contains information regarding the excitation of the core electron of which the white line, the initial intense peak[15] of the spectrum, which is typically correlated to the oxidation state of the material.

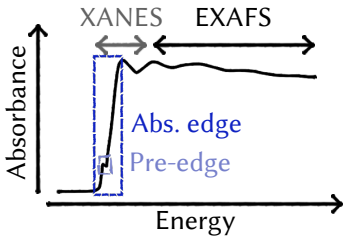

Figure 3.11: A schematic XAS spectrum showcasing the X-ray absorption fine structure with its absorption edge and the XANES and EXAFS regions.

15: With an emphasis on intense, there can be minor features which appear prior to this white line, referred to as pre-edge peaks. These can be composed of excitations of core electrons into a lower energy levels.

In this study, the rhodium and palladium based catalysts have been studied by *in situ* and *operando* XAS respectively. These studies were carried out at Insertion device 24 (ID24) in the European Synchrotron Radiation Facility (ESRF), Grenoble France. While XAS is a highly information rich method, we have in this study limited the scope of the analysis and primarily used it to obtain the oxidation state of the catalysts transiently.

Elemental composition: X-ray fluorescence spectroscopy

In addition to structure, we may deduce the atomic composition of a material using X-rays. As already stated in the XPS and XAS sections, it is possible to excite an atoms electrons by the absorption of X-ray. As for the case of XPS, given that the material is exposed to X-ray greater than its ionization energy, this excited electron enters the continuum and is ejected from the atom. In a response to this, the atom may emit one or more photons, letting electrons of higher orbitals fall into lower ones, refilling the core electron holes.[71] This emission of radiation due to excitation by radiation absorption is called fluorescence. By measuring the energy and intensity of the emitted radiation, it is possible to quantify the amount (by intensity) and type of atom (energy).[71] This X-ray fluorescence (XRF) can typically be studied in combination with X-ray absorbing experiments such as XPS and XAS. In this work however, this has been performed standalone using a PANalytical axios spectrometer (Malvern) with the purpose of deducing the composition of the studied catalysts.

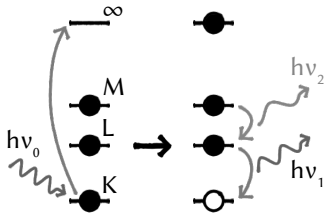

Figure 3.12: Schematic drawing of the X-ray fluorescence process, showing a single electron from the K, L and M shell each. The core electron is excited into the continuum and the loss of this electron makes the electron structure unstable. As a response, the electrons from the M and L shells may relax to lower energy state, releasing photons in the process.

3.5 Probing catalyst adsorbates by infrared spectroscopy

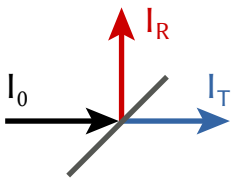

Figure 3.13: Schematic representation of transmission and reflectance

There are a few ways photons may interaction with matter, namely by being scattered, reflected, transmitted, or absorbed by the material. While the first named properties are useful to determine structure and shape of a material, absorption may instead allow one to study the chemical state due to its relation to effects such as electron excitation. However, unlike absorption of more energetic radiation, such as visible light, infrared light typically has a too low energy as to cause electronic transitions and instead is limited to the excitation of molecular vibrational states.[72] By visualising these vibrations as harmonic oscillator, of which a two-point spring would be the simplest model, one realises that the different functional groups of a molecule can be distinguished by their absorption energies, as they posses different geometry, bond strength and mass. However, not all groups can be studied by IR spectroscopy. In order for a vibration to be "IR active", it has to induce a net change in the dipolar moment of the group.[73] As an example, in Table 3.1 the six normal modes of vibrations are applied to CO_2. While being able to produce both a symmetrical as well as an asymmetrical vibration, for the symmetrical case the change in dipole moment for each individual bond cancel each other out, and as such this vibration will be invisible to IR while the asymmetrical vibration allow for an absorption of the IR light.

Table 3.1: The six normal modes of vibration, applied to the CO_2 molecule, with the net change in dipole moment, $\Sigma\vec{\mu}_i$. Note that of these 6 vibrations only 3 are observed for CO_2 as ρ and τ are rotations for CO_2 and ν_s is IR inactive due to lack of net change in dipole moment.

Stretching		Bending			
		In-plane		Out-of-plane	
ν_s (Symmetric)	ν_{as} (Asymmetric)	δ (Scissoring)	ρ (Rocking)	ω (Wagging)	τ (Twisting)
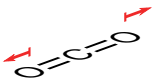			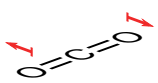	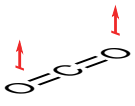	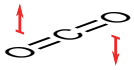
$\Sigma\vec{\mu}_i = 0$	$\Sigma\vec{\mu}_i > 0$	$\Sigma\vec{\mu}_i > 0$	$\Sigma\vec{\mu}_i = 0$	$\Sigma\vec{\mu}_i > 0$	$\Sigma\vec{\mu}_i = 0$

$$T = \frac{I_0}{I_T} \tag{3.26}$$

$$A = \log_{10}\frac{1}{T} \tag{3.27}$$

$$R = \frac{I_0}{I_R} \tag{3.28}$$

$$A' = \log_{10}\frac{1}{R} \tag{3.29}$$

T : Transmittance
R : Reflectance
I_0 : Intensity of incident light
I_x : Intensity of transmitted (T) or reflected (R) light
A : Absorbance
A' : Pseudo absorbance

As for the study of absorption spectroscopy, it is foremost the transmission (T) and reflection (R) that is taken into regard whereas scattering effects are minimised and neglected. The quantitative expression of transmission spectroscopy follows equation (3.26) where the intensity of the incident light (I_0) is divided by the intensity of the transmitted (I_T) light (or if measured in reflection mode, the reflected light, I_R).[72,74] The absorption of the light is expressed as absorbance (A), which is either the logarithm of the reciprocal transmission or reflectance of the light as expressed by equation (3.27) for transmission. Typically, infrared spectroscopy is measured by interferometry, in which a large span of wavelengths are measured simultaneously while modulating their phase shifts, resulting in a pattern of constructive and destructive interference (an interferogram). Using Fourier transform, a spectrum can be obtained from this interferogram. This Fourier transform infrared (FT-IR) spectroscopy provides dramatically higher spectrum sampling rates compared to measuring individual wavelengths.[16]

16: Making it so widely adopted that it is colloquially simply known as IR spectroscopy, leaving the Fourier transform portion implicit.

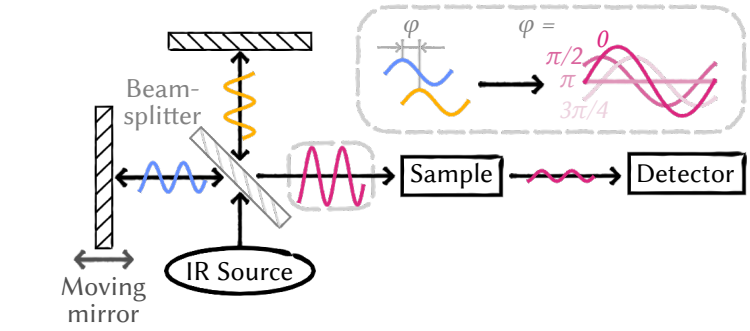

Figure 3.14: Infrared measurement by interferometry. The inset highlights the change in shape and intensity of the probing light, due to the controlled interference by the moving mirror, which gives the resulting interferogram.

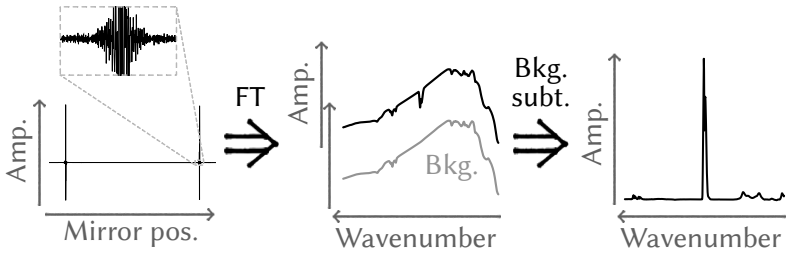

Figure 3.15: The steps of the data processing of FT-IR data, from the interferogram from the measurement, to the solved transmission/reflectance spectrum and finally the absorbance spectrum in which a background subtraction has been performed.

When measuring the absorbance, typically either only transmission or reflectance is accounted for and in the case of a reflectance measurement, the absorbance is often referred to as a pseudo-absorbance[17].

17: In this work denoted as A', $\log \frac{1}{R}$ or simply "log reflectance", leaving the reciprocal as implicit

Diffuse reflectance

Being presented with the concept of reflection of light, it is perhaps that of a mirror which comes to mind. This kind of reflection is referred to as specular reflection and occurs on fine surfaces, such as those of ordered crystals and smooth materials like metals and glasses. Light which is specularly reflected appears at the same angle as that of the incident light, in regards to the normal. However, the more common mode of reflection of light is the diffuse reflection, which like its name suggests produces a randomly distributed reflection, as illustrated in Figure 3.16. While on a microscopic scale behaving in the same manner as specular reflection, this macroscopic observation is due to a multitude of different, non-aligned, reflection surfaces being present, be it due to the polycrystallinity and/or surface roughness of the material.[74]

For infrared spectroscopy measurement modes such as transmission and specular reflection, this diffuse reflection is detrimental to the study as light may become lost due to other effects than absorption. However, one can instead utilise this reflectance mode, as is the case for Diffuse Reflectance Infrared Fourier Transform Spectroscopy (DRIFTS). By letting the material act as its own mirror and have the light propagate through it, interacting with multiple surfaces and adsorbates on the way, and recording the light reflected back the occurred absorption can be obtained.[18] Indeed, this eliminates the sample preparations involved for the transmission and specular reflection modes, which like in this study allows for the study of a catalyst powder sample.

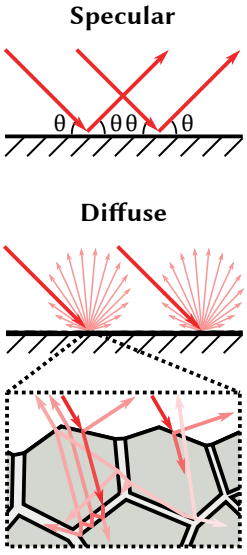

Figure 3.16: Schematic illustration for the difference between specular and diffusive reflection. The "zoom" is an example of some internal reflections of a polycrystalline material.

18: Given that this light is gathered from several angles, such as by the usage of concave mirrors, to account for its spread.

In this work, infrared absorption has been recorded using a VERTEX 70 and v80 (Bruker) together with a Praying Mantis™ DRIFTS mirror cell (Harrick) and its high temperature reaction chamber[19] have been used to perform the DRIFTS study. This sample chamber suffers from a significant dead volume, previously discussed in Section 3.3, as well as a discrepancy between cell and sample temperature.[75] In this work, in order to decrease the error in temperature, a thermocouple was fed through the exhaust port into the sample.

19: For which a part of the reaction chamber is schematically drawn in Figure 3.17.

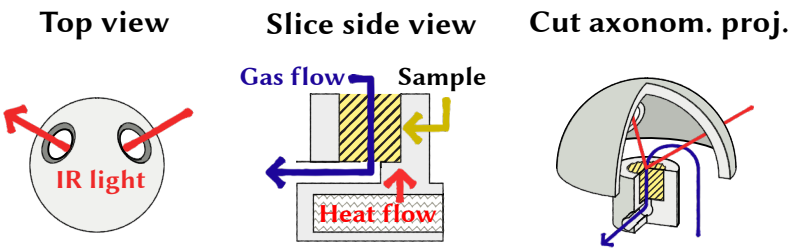

Figure 3.17: Schematic illustration of the DRIFTS cell set-up, showing the dome and sample cup without surrounding enclosure. Note that the light does not travel in a straight line through the dome, as to reduce the amount of specular reflection.

Peak profiles and deconvolution

As often is the case for infrared spectroscopy, the resulting peaks of the vibrations in the spectrum become convoluted, complicating or prohibiting one to compare their amount and occurrence. In order to circumvent this one may employ deconvolution, describing the spectrum as a sum of line profiles. The choice of profiles for the fit is dependent on the broadening of which there are primarily two contributors to take into regard, natural relaxation and pressure broadening (in which the frequencies are spread due to collisions and the vibrations become incoherent).[76] For solids, one may expect a low molecular movement and as such the pressure broadening can be ignored, resulting a fully Gaussian profile. For gases it is instead the opposite, the fast movements and high frequency of collisions makes the pressure broadening the dominant contributor, giving a Lorentzian profile. For intermediate conditions, such as liquids, the profile thus has both Gaussian and Lorentzian components, which can be described by a Voigt profile,[20] shown in equation (3.32), which is a convolution of the Gaussian and Lorentzian.

In this work, Voigt profiles have been used for the fitting of adsorbates in order to include the influence of potential surface diffusion and adsorbate-adsorbate collisions which may occur and perturb the otherwise predominantly Gaussian profiles of the adsorbate vibrations. These fittings were done for CO adsorption on the Pd samples in order to solve the F_s parameter of the chemisorption analysis (see page 9).

The Gaussian and Lorentzian profiles.

$$G(x;\sigma) \equiv \frac{\exp\left(-(x-\mu)^2/(2\sigma^2)\right)}{\sigma\sqrt{2\pi}} \tag{3.30}$$

$$L(x;\gamma) \equiv \frac{\gamma}{\pi((x-\mu)^2+\gamma^2)} \tag{3.31}$$

μ : Centre point
σ^2 : Variance
2γ : Full width at half maximum

20: Or by a less accurate but computationally less demanding pseudo Voigt.
$PV = (1-x)G + xL \qquad x\epsilon(0,1)$

$$V(x;\sigma,\gamma) \equiv \int_{-\infty}^{\infty} G(x';\sigma)L(x-x';\gamma)\,\mathrm{d}x' = \frac{\mathrm{Re}[\omega(z)]}{\sigma\sqrt{2\pi}} \tag{3.32}$$

For which $\omega(z)$ is the Faddeeva function

$$\omega(z) = e^{-z^2}\left(1 + \frac{2i}{\sqrt{\pi}}\int_0^z e^{t^2}dt\right) \tag{3.33}$$

On the mechanisms of methanation by rhodium

4

In regards to the study of the function of a catalyst, there are two interlinking aspects to consider — the behaviour of the catalyst material, and the surface reaction. In Paper I and II, we explored the change in crystal structure and oxidation state of the Rh/Al_2O_3, Rh/SiO_2, and Rh/CeO_2 catalysts, and made a brief analysis of formed surface adsorbates. Due to some ambiguities regarding the adsorbates of the CeO_2 based catalysts, a more in depth study focused solely on the surface reaction was performed in Paper III and V. In these studies, the catalyst was studied in the temperature span of 200-350 °C. The importance of this span, as reported in a previous kinetic study,[77] is the initiation of CO (g) formation at a temperature between 250 and 350 °C whereas CH_4 (g) production occurs in the entire temperature interval.

The main finding was that although all catalysts seem to follow a pathway with CO as principal reaction intermediate, the CeO_2 phase of Rh/CeO_2 showed activity during the hydrogenation. However, while it still remains unknown whether this activity is due to only a side reaction on CeO_2, the presence of CO at the Rh-CeO_2 rim or a different behaviour of the CeO_2 phase between the pure ceria and the one with Rh, the activity suggests that CeO_2 might take a direct role in the methanation reaction.

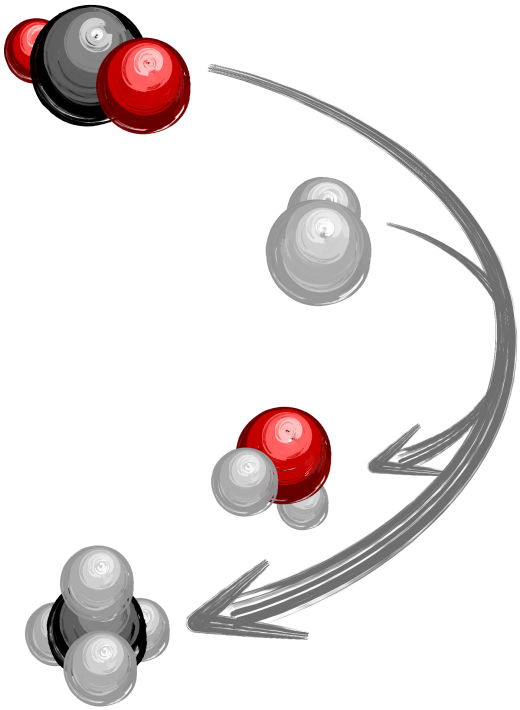

4.1 The case of irreducible supports – Rh/Al_2O_3 and Rh/SiO_2

In a previous work, it was shown that Rh/Al_2O_3 displayed a higher activity for CO_2 methanation than Rh/SiO_2.[77] In order to explore the behaviour of these catalysts, which in turn could provide support in forming an idea for their reaction mechanisms, *in situ* ED-XAS and HE-XRD in a MES manner as well as steady-state DRIFTS were employed. In order to study the oxidation state of the catalysts during the reaction, the XAS study began with obtaining references for the reduced and oxidised states. Following this, the oxidation state was studied and a MES approach was taken to gain an insight into the transient behaviour of the catalyst. After gaining this understanding of the oxidation state, the structural change was studied by HE-XRD. Lastly, the adsorbates at steady state condition was studied by DRIFTS. These methods were previously described in the Sections: Oxidation state: X-ray absorption spectroscopy (p. 14), Separating active species from spectators by modulation excitation (p. 10), Crystal structure: X-ray diffraction (p. 13) and Probing catalyst adsorbates by infrared spectroscopy (p. 16) respectively.

Establishing a reference – Study of redox behaviour

To act as a reference for the study of the catalysts during the methanation reaction, the oxidation states of the catalysts were studied by XAS in an oxidising (feed of 2 vol.% O_2) and reductive environment (feed of 2 vol.% H_2) at 350 °C, in steps of 4 min. The transient redox behaviour of the Rh/Al_2O_3 catalyst can be seen in Figure 4.1, in which the white line intensity (WLI) is used to illustrate the oxidation state.[1] While initially showing a sharp increase in WLI as O_2 is introduced, its rate later on tapers off. This observed behaviour presumably originates from a rapid oxidation of the surface Rh, followed by a sluggish bulk oxidation. Later when O_2 is removed and H_2 is introduced a near instantaneous drop is seen for the WLI. As such, at least for the particle surface of Rh, a swift oxidation/reduction is expected. Furthermore, as the WLI remains stable during the O_2/H_2 cycling, a particle growth is not expected to have taken place.

Similar transient behaviour to that of Rh/Al_2O_3 at 350 °C was also seen at 250 and 300 °C as well as for Rh/SiO_2 catalyst at these temperatures. As such, only the state of the oxidised and reduced sample is displayed for the remaining experiments. The XANES and EXAFS of the reduced and oxidised state of both Rh/Al_2O_3 and Rh/SiO_2 at 250, 300 and 350 °C are presented in Figure 4.2. As previously seen in Figure 4.1, an elevated WLI is shown for reduced samples in the XANES spectra (left column, Figure 4.2), whereas a decrease is exhibited for the oxidised case. Curiously, the WLI of Rh/SiO_2 at 350 °C is quite prominent in comparison to the other temperatures. As for the cause of this, some likely explanations are the formation of a thicker oxide layer and/or a change in particle size.

In support of the XANES analysis, the local structure of the Rh atom was studied by a qualitative EXAFS analysis (right column, Figure 4.2).[2] It was primarily two kinds of coordination shells that was found, that of

1: The WLI was deemed an appropriate descriptor as the Rh K-edge is directly related to the density of vacant d-orbital states of Rh. However, caution is needed when using WLI as oxidation state descriptor as other factors such as particle size can also show a contribution.[78,79]

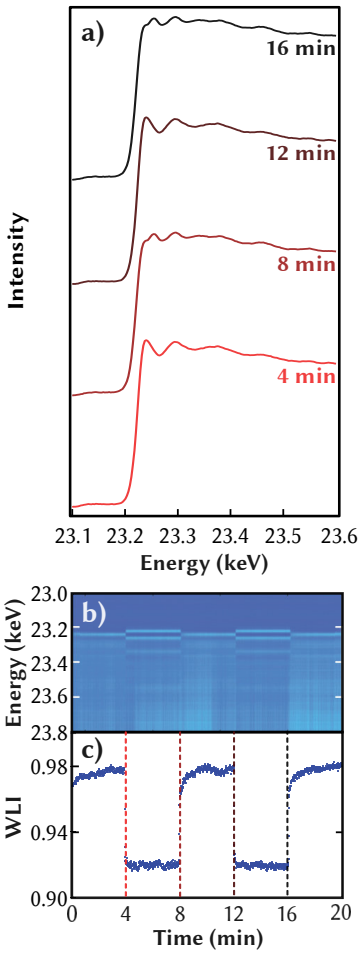

Figure 4.1: XAS spectra of the Rh K edge of Rh/Al_2O_3 during O_2/H_2 cycling at 350 °C. The oxidation (2 vol.% O_2) and reduction (2 vol.% H_2) steps had a length of 4 min and started with O_2. The XAS spectra at the end of the O_2/H_2 step, a), as well as contour plot of the difference spectra (i.e. the initial spectrum have been subtracted from each individual spectrum of the data set), b), and the white line intensity at 23.24 keV (c) against time is shown. The first step is that of O_2 introduction.

2: Regarding the EXAFS data, as no phase shift correction was performed on the data, the shown distances are shorter than what is expected for the real case.

Rh-Rh and Rh-O seen as peaks in the EXAFS spectra at 2.57 and 1.94 Å respectively.[80–82] Although the catalysts experienced a rapid reduction followed by a constant oxidation state, i.e. no slow bulk reduction, the presence of Rh-O can still be observed for both catalysts at all temperatures at the end of the reduction step. This signifies that a portion of the Rh particle is irreducible under these conditions. Likewise, the oxygen treatment did not fully oxidise the sample, as evidenced by the presence of Rh-Rh. Indeed, the expected peaks of Rh-O-Rh [3] are absent in the spectra, suggesting that only a surface level of Rh-O is present, as well as a Rh-O contribution from the Rh-support interaction. As for the lower Rh-Rh to Rh-O ratio for Rh/Al_2O_3 compared to the case of SiO_2, a possible explanation is a stronger metal-support-interaction for this catalyst which in turn prevents a larger volume of the Rh phase from being reduced. However, the lack of a Rh-O-Al shell[4] suggests that the metal-support-interaction is still relatively weak compared to, for example, aged alumina-supported Rh as well as ceria-supported Rh who have shown such contributions.[80–83] Furthermore, a larger particle size of Rh on SiO_2 compared to Al_2O_3 could also contribute to this difference.[5]

3: Which for the case of Rh_2O_3 is expected at 2.7 and 3.3 Å. Certainly, while other RhO models could provide other scattering values there is nevertheless a lack of clear peaks except those of Rh-Rh and Rh-CO. Of course, there are some minor peaks present in the spectra but it is uncertain if these are real or simply "ghost peaks".

4: Which should have given rise to a double peak at $R \sim 2.5, 3$ Å[80–82]

5: Given that only surface atoms become oxidised it would then simply be a difference in surface-to-volume ratio.

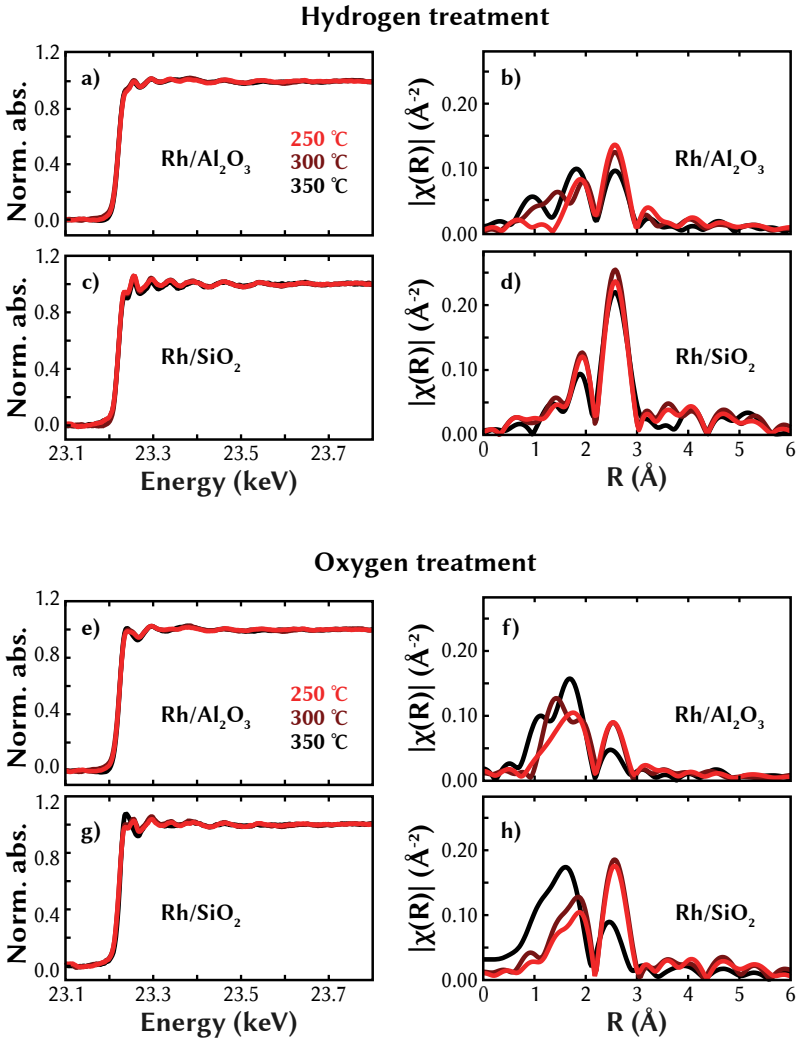

Figure 4.2: *In situ* XAS spectra (XANES and EXAFS in left and right column respectively) of the Rh K edge of Rh/Al_2O_3 Rh/SiO_2 catalysts at 250, 300 and 350 °C at the end of the reducing hydrogen (2 vol.% H_2) and oxidising oxygen (2 vol.% O_2) steps.

The state of the catalyst during hydrogenation

Having established the basic redox behaviour of the catalysts, an *in situ* ED-XAS study of the methanation reaction was performed at 250, 300 and 350 °C as well as an *in situ* HE-XRD at 350 °C, utilising a MES approach in which H_2 was periodically introduced and removed from a constant CO_2 stream[6].

6: Alternated between and 2 vol.% H_2 + 0.5 vol.% CO_2 and 0.5 vol.% CO_2 with a pulse length of 10 min. For the HE-XRD, 5 cycles were performed, giving a total time of 100 min.

Oxidation state dynamics from ED-XAS

By comparison of the WLI in XANES of the catalyst during methanation, see Figure 4.3, with the previously produced reference, the catalysts appear to be in a predominately reduced state. However, while only a slight shift could be seen in the XANES spectra during the H_2 cycling, the EXAFS displayed a clearer picture. Although only a negligible difference could be seen for the intensity of Rh-Rh and Rh-O during H_2 cycling, a clear shift of the Rh-Rh / Rh-O ratio is seen as the temperature is increased. While displayed for both catalysts, it is most apparent for Rh/SiO_2. As previously stated for the reference cases, a metal-support interaction is expected to compose a part of the Rh-O scattering and as this contribution is expected to be near constant[7] this change of Rh-O is thus likely due to a growth and consumption of an oxide layer on the metal particle. However, since only a minor change is seen for Rh-Rh, no thick oxide layer is expected. Furthermore, comparing the alumina and silica catalysts, it seems as though the Rh on silica is less oxidised than that of Rh on alumina.

7: Unless the interaction volume between the particle and support changes, for example by a change in particle size and shape which would change the number of metal atoms in contact with the oxide of the support. A spherical particle flattening and wetting the surface would be an example of this. As such, while the increased WLI for Rh/SiO_2 could be explained by a particle size increase, this alone could not indicate an increased Rh-O contribution from the metal-support interaction as it does not necessitate an increased contact area with the support which results in Rh previously unexposed to the support now being in contact with the oxide.

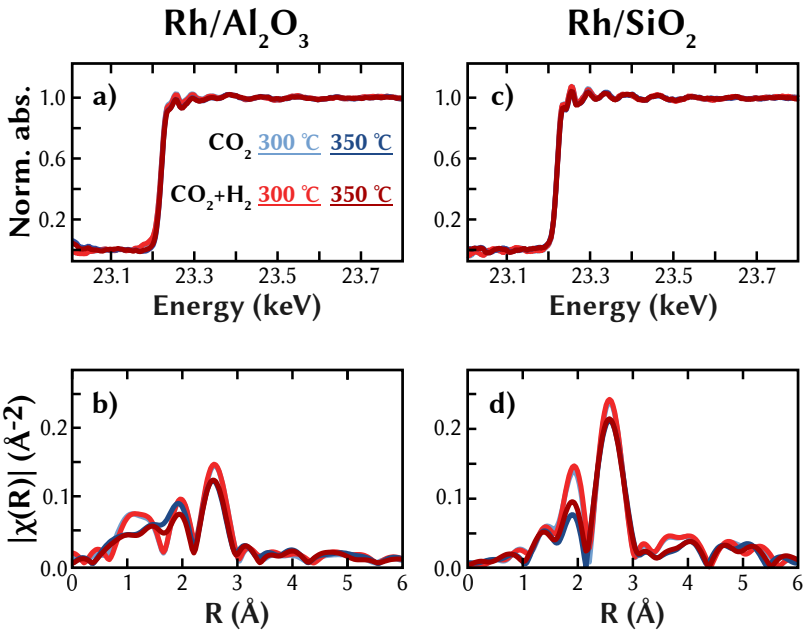

Figure 4.3: XAS spectra of the Rh K-edge of $RhAl_2O_3$ and Rh/SiO_2 catalysts (column-wise) during methanation, displayed as XANES (upper row) and EXAFS spectra (bottom row).

Observing changes in crystal structure by HE-XRD

Apart from an initial jump, the XRD pattern did not reveal any significant changes of the alumina phase. Furthermore, no peaks of pure Rh metal were seen, however, a weak reflection at $q = 2.85$ Å displayed a cyclic response to the H_2 stimulus. The application of Bragg's law on this peak yields an interplanar distance of $d = 2.20$ Å[8] which when compared to the d value for Rh, Rh_2O_3 and RhO_2[9] suggests that the Rh does not adopt an oxide structure and is partially oxidised into RhO_x, predominately being composed of metal Rh as suggested by the heavy shift of the peak to that of Rh and the previous ED-XAS study.[10] Based on these findings by XRD and XAS, a CO_2 dissociation into $CO_{ads.}$ and $O_{ads.}$ is most likely taking place on the rhodium metal.

Upon the introduction of H_2, the broad RhO_x sharpens, which could be attributed to an increased crystallite size. However, another explanation would be that of the adoption of a more well-ordered state. As an example, given that this peak originated from a Rh-RhO_x mixture, this could be realised as a growth of a well-ordered Rh metal core at the expense of a less ordered RhO_x as well as a potential amorphous region between these two phases.

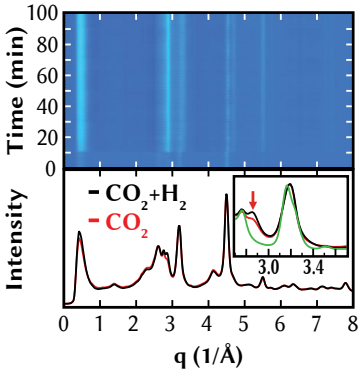

Figure 4.4: The XRD pattern of Rh/Al_2O_3 against time and at the end of a CO_2 step (red) as well as CO_2+H_2 (black together with a reference alumina pattern (green). Highlighted in the inset is the oscillating 2.85 Å peak.

8: Given a wavelength of $\lambda = 0.155$ Å

9: See Table 4.1 for some selected planes of Rh, Rh_2O_3 and RhO_2 with the closest match to the observed peak.

10: Also keep in regard that XRD is limited to structures of long range order, there may also be amorphous phases which are undetectable by this method. Likewise, small particles might also remain undetected.

Table 4.1: Crystal planes of Rh, Rh_2O_3 and RhO_2 most closely matching the observed oscillating peak in Figure 4.4.

Plane	d (Å)	ICSD ref.[84]
Rh		
(111)	2.07	# 171677
Rh_2O_3, orthorhombic		
(020)	2.7	# 41534
RhO_2		
(111)	2.8	# 251565

Surface species

In order to provide a link between structural change and surface reactions, a brief DRIFTS study of steady-state reaction at 350 °C was performed.[11]

While both samples displayed the formation of carbonyls, as seen in Figure 4.5, of linear (m-CO, 2020 cm^{-1})[85] and bridged (br-CO, 1780 cm^{-1})[86] configuration, mostly m-CO accumulated on the Rh/Al_2O_3 catalyst whereas instead br-CO was the favoured adsorbate for Rh/SiO_2.[12] As for the reason behind this difference, it could be due to the catalysts structural differences as other studies have shown that br-CO is favoured on larger particles,[87] but it could otherwise be due to kinetics. Contradictorily, these build-ups may both suggest that m-CO and br-CO is the primary intermediate while the other one is of a slower pathway or even a spectator. Given that m-CO is the main intermediate, the higher m-CO coverage on Rh/Al_2O_3 would be correlated to the faster kinetics of this catalyst, allowing the adoption of this configuration or a much faster production rate. The br-CO would then simply be a stagnant spectator, which while formed does not participate. On the other end, not only the rate of formation but also that of consumption would be expected with an increased overall reaction rate. As such, this large accumulation of m-CO could point toward this adsorbate not showing a participation in the reaction. While the same is not seen for the case of Rh/SiO_2 would then be explained by the previously presented findings regarding configuration and particle size, this particle simply does not accommodate the surfaces for which m-CO would accumulate, preventing the large build up seen on Rh/Al_2O_3. Indeed, this idea could be supported by the study of Karelovic *et al.* in which br-CO was found to have a higher activity than m-CO at lower temperatures (150-200 °C).[85] As such, while not providing a definite way to determine the principal intermediate, these results point toward a potential follow up study.

11: Using lower concentrations than the XAS and XRD study, 0.2 vol.% CO_2 and 0.8 vol.% H_2, in order to more easily separate peaks and avoid convolution. Of course, one may instead miss species which require a higher reactant coverage in order to accumulate, but a deconvolution might be needed in order to distinguish these anyway. The steady-state spectra were recorded after 20 min of reactant gas exposure.

12: What is not shown is the case of CO_2 adsorption without H_2. Only minimal peaks, likely only formation of carbonates, were present on the surface without the inclusion of H_2.

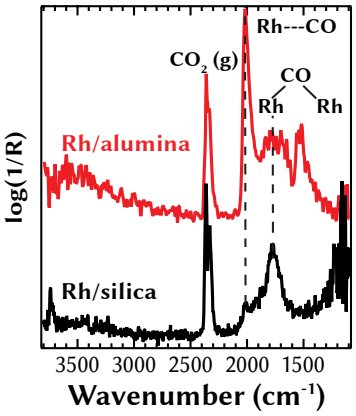

Figure 4.5: DRIFTS spectra of Rh/Al_2O_3 (red) and Rh/SiO_2 (black) after 20 min exposure to a flow of 0.2 vol.% H_2 and 0.8 vol.% H_2 at 350 °C.

While adsorbates such as m-CO and br-CO shown by DRIFTS, no C−H (2800-3000 cm^{-1}) nor CO on Rh^+ sites were seen. As such, neither formates nor CO at oxidised Rh are not expected to have been formed or participate in the reaction. For the case of formates, due to often being a quite stable adsorbate, making its hydrogenation a rate limiting step (and should therefore accumulate).

Putting it all together

It was shown by XAS and XRD that while being predominately reduced, there is an oxide phase on the Rh particles during the methanation reaction. This coupled with the DRIFTS study of catalyst adsorbates during the reaction suggests that CO_2 dissociates on the Rh particles, forming m-CO and br-CO as well as oxygen adatoms, which in turn contributes to the oxidation of the catalysts. As no other adsorbates were present, the reaction is expected to proceed using CO as a principal intermediate, following a reaction route such as the carbide pathway. Furthermore, lacking CO species which could be contributed to CO at a reduced Rh site, Rh^0 is expected to be the active site of the reaction.

4.2 The case of a reducible support – Rh/CeO$_2$

Having established that the methanation on rhodium appears to follow a carbon monoxide based pathway on Rh/Al$_2$O$_3$ as well as Rh/SiO$_2$, the structural behaviour and surface reactions of Rh/CeO$_2$ were studied. The introduction of a reducible support is interesting in regards to its mechanistic study, as the support itself may display separate mechanisms. Furthermore, this would also create intermediate regions where the domain of the metal particle and support meet, exhibiting behaviour that is distinct from both but still being dependent on them. Indeed, this could potentially be related to the higher activity seen for Rh/CeO$_2$ than Rh/Al$_2$O$_3$ and Rh/SiO$_2$.[77] As such, like the for the previously studied rhodium catalysts with irreducible supports, this study began with a characterisation of the structural behaviour and then a study of the surface adsorbates during reaction of which this catalyst was subjected to a more in depth study.

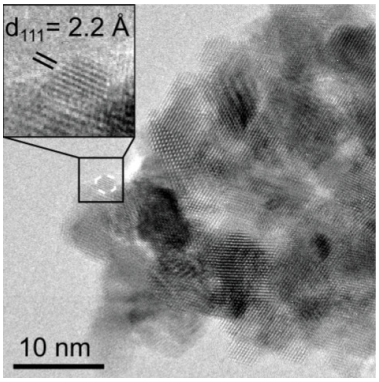

Figure 4.6: High-resolution TEM image of the Rh/CeO$_2$ catalyst used in the *in situ* structural study. The inset shows a 2 nm Rh crystallite, showing the 2.2 Å interplanar distance of the (111) plane.

Physico-chemical behaviour of the catalyst

In order to probe for the possibility of formation of new catalyst compounds during the reaction, such as oxides and carbides of the active metal, HE-XRD was performed. By this method the bulk phases of material domains with sufficient long range order can be studied *in situ*. Furthermore, AP-XPS was performed in order to observe changes in oxidation state of the surface *in situ* upon exposure to reaction atmospheres.

Observing the crystal structural dynamics

The crystal structural dynamics of the Rh/CeO$_2$ catalyst was studied by transient *in situ* HE-XRD using a modulation excitation approach (see Section 3.3). While the sample was exposed to a constant CO$_2$ flow (0.5 vol.%), the H$_2$ concentration was periodically changed between 0 and 2 vol.% in a square-wave fashion (20 min period time) while the diffractogram of the sample was recorded. The resulting diffractograms can be seen as difference plots in Figure 4.7. While weak, a peak corresponding to supported rhodium metal (Rh$_{supp.}$) is observed during these experiments. This reflection corresponds to a d spacing of 2.2 Å, whereas 2.1 Å is expected for metallic Rh, which is likely due to a strong interaction with CeO$_2$ and possibly also with a boundary RhO$_x$ phase as observed with AP-XPS (discussed later). As for the lack of strong rhodium peaks, this is likely due to a combination of amorphous rhodium metal and small particles (of which particle diameters of 2-3 nm were largely observed in TEM, with an average of 4 nm), for which both of these factors create a lack of well defined long range order. While no change in regards to rhodium is observed during this experiment, a decrease in q for the reflections of CeO$_2$ during CO$_2$ hydrogenation could be clearly seen. This decrease in q corresponds to an increase in interplanar distances (d), which in turn suggests an expansion of the unit cell. While this reduction is expected, the partial re-oxidation of CeO$_2$ following the removal of H$_2$ (increase in q) from the gas stream provides a new insight to the reaction. Namely, it suggests that either CO$_2$ itself or

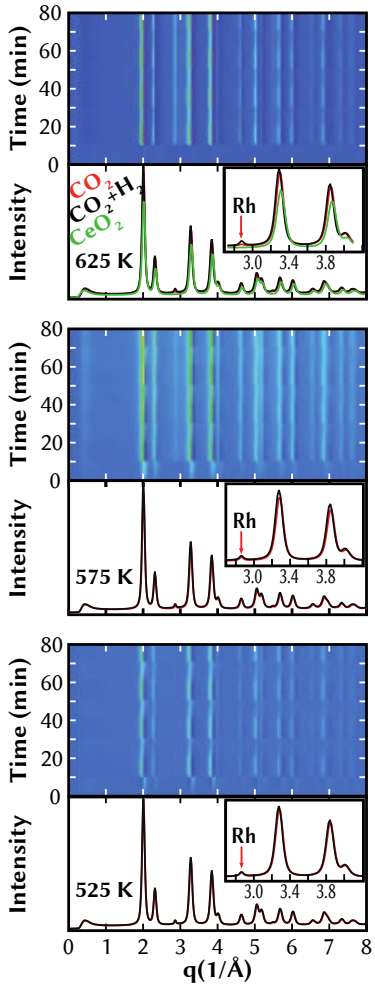

Figure 4.7: X-ray diffractograms of Rh/CeO$_2$ during CO$_2$ hydrogenation with H$_2$ pulses with an inset showing the peak of Rh$_{supp.}$ (marked 'Rh'). In the contour plot, the initial pattern has been subtracted from the series.

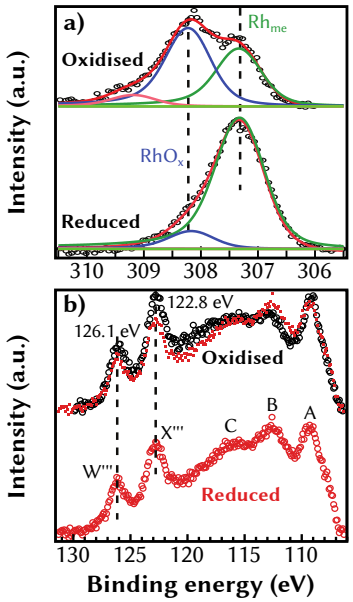

Figure 4.8: XPS spectra of Rh 3d (a) and Ce 4d (b) for reduced and oxidised Rh/CeO_2. Red squares in (b) is reduced Rh/CeO_2.

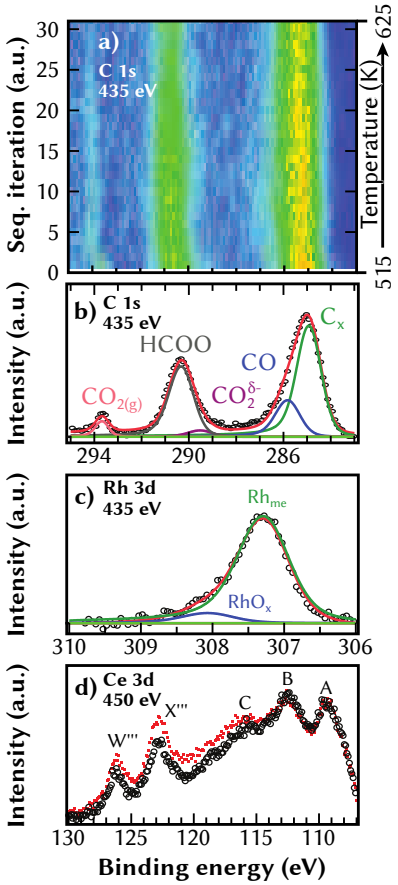

Figure 4.9: XPS spectra of Rh/CeO_2 during CO_2 methanation, showing C 1s during the temp. ramp (a) as well as C, Rh and Ce (b-d) at 515 K.

remaining reaction intermediate(s) from the hydrogenation reaction to some extent heals the oxygen vacancies formed at CeO_2. This shows that the redox behaviour of CeO_2 could be involved in the catalytic reaction mechanism, its role in the CO_2 methanation and rWGS reactions cannot be determined from this experiment alone.

Changes in the surface oxidation state

The oxidation state of the catalyst surface was explored using AP-XPS. As seen in Figure 4.8, both RhO_x and Rh metal phases with alternating ratios of the oxidised and reduced state are observed when the Rh/CeO_2 sample held at 595 K is exposed to a hydrogen (1.33×10^{-6} hPa) and oxygen (1.33×10^{-5} hPa) environment, respectively. Furthermore, the rhodium is not fully reduced under the hydrogen conditions. Similar to what is observed in the HE-XRD measurements, a partial reduction of CeO_2 is seen in the reducing environment as a decline of Ce^{4+} signal.

As for *in situ* study of the methanation using AP-XPS, a transient study was performed in which the sample was exposed to a gas mixture of 0.0133 hPa CO_2 and 0.1867 hPa H_2 and the temperature was gradually increased from 515 to 625 K. Like the previous reduction-oxidation experiment, rhodium remains as partially oxidised during the experiment. As for the C 1s region, formation of surface species such as HCOO and CO is seen. While present on the surface at 515 K, no CO (g) was detected by the mass spectrometer while CH_4 production was seen during the whole temperature range. The first CO (g) could not be observed until 615 K was reached.

Exploring the surface reactions

While the previous AP-XPS results show that CO and HCOO species form on the Rh/CeO_2 catalyst, the possibility of them being intermediates could not be ascertained. As such, this was followed by a study focused solely on the surface reactions by the use of DRIFTS. An initial assessment of the surface adsorbates during reaction conditions was performed by steady-state hydrogenation at 200, 250 and 300 °C. Afterwards, the hydrogenation was studied transiently at the same temperature in order to deduce which of the adsorbates that correspond to intermediates.

Active and inactive, adsorbates at steady-state

After exposing Rh/CeO_2 to a flow of 0.5 vol.% CO_2, carbonate (CO_3) formation is observed out of which bidentate (b-CO_3) is the primary mode of adsorption of CO_2 to CeO_2, see Figure 4.10a. After the introduction of 2 vol.% H_2 to the CO_2 stream, additional peaks with high absorption appeared. Based on that these peaks correspond to hydrogenation products and the previous observation of HCOO in the AP-XPS experiment, one would expect that the peaks in the 1600-1300 cm^{-1} region would correspond at least partially to HCOO. However, although C−H vibrations for HCOO are weaker than those of O−C−O, the weak C−H vibrations in the 2900-2800 cm^{-1} region signifies that HCOO only constitutes a minor portion of the peaks in the 1600-1300 cm^{-1} region. As for the prominent

peak at 1744 cm^{-1}, its high wavenumber suggests a carbonyl such as a bridged CO which is further supported by its temperature dependence. While showing some discrepancy (reference value: 1725 cm^{-1}[88]) to previous assignments, this peak is likely primarily composed of CO located at the interface of Rh and CeO_2 (ν(C=O)$_{Rh\text{-}CeO_2}$). As for the mode of coordination, it has been suggested that the CO adopts a Rh−C=O−Ce coordination[13] in which the oxygen is coordinated to a Lewis acid site of the support.[88] As for the higher wavenumber of this peak compared to the reference, this is possibly due to additional convoluted vibrations in the peak. Furthermore, minor peaks corresponding to species such as m-CO can be seen in the shoulder towards higher wavenumbers.

13: Here given as a general description. The number of co ordinations to Rh varies and has been for example suggested to actually be Rh_3−C=O−Ce.

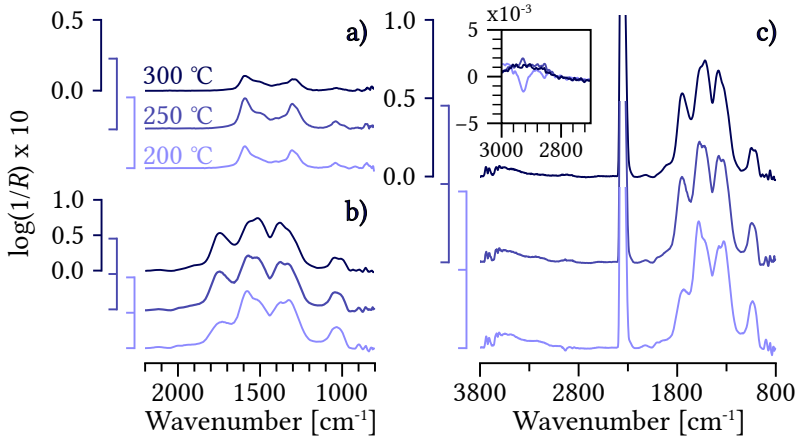

Figure 4.10: Steady-state *in situ* infrared spectra for the Rh/CeO_2 catalyst at the studied temperatures in the carbon-oxygen bond region 2200-800 cm^{-1} during (a) CO_2 adsorption (y_{CO_2} = 0.5) and (b) hydrogenation (y_{CO_2} = 0.5, y_{H_2} = 2) as well as the complete measured region with a zoom at the C-H bond region 3000-2550 cm^{-1} during hydrogenation (c).

After increasing the gas concentrations to 1 vol.% CO_2 and 4 vol.% H_2, the O−C−O and C=O peaks show a sizable growth as seen in Figure 4.11. However, the C−H peaks remain at a insignificant level. As such, if formates are present, as suggested by the previous XPS study, these steady-state measurements suggests that their coverage is minimal.

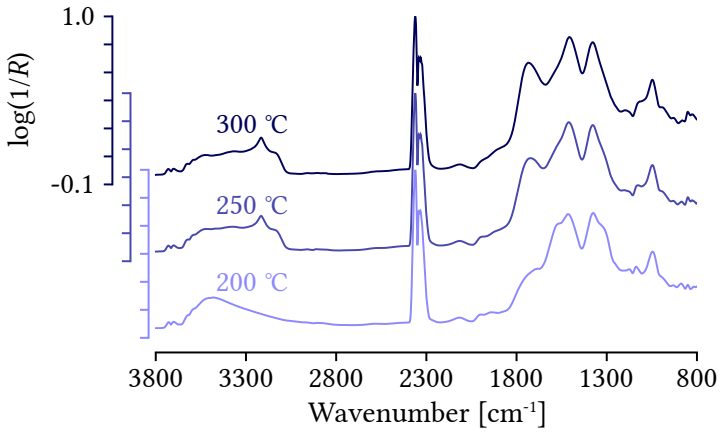

Figure 4.11: *In situ* infrared spectra collected during steady-state hydrogenation reaction conditions at increased gas concentration, i.e., 1 vol.% CO_2, 4 vol.% H_2. The spectra have been normalised such that the intensity of the 2360 cm^{-1} peak is equal to 1. Unlike the steady-state measurement at lower concentrations, shown in Figure 4.10 c, no H_2 pre-treatment was performed prior to the background collection of these measurements. As such, hydroxyls and adsorbed water are more prominent in these spectra as portions of them are not hidden in the background.

In order to more easily separate adsorbates on the Rh surface to that of CeO_2, reference measurements of CO_2 adsorption and steady-state conditions[14] on pure CeO_2 were studied and their DRIFTS spectra can be seen in Figure 4.12 and 4.13 respectively. Unlike the case of Rh/CeO_2, the dominant mode of adsorption on CeO_2 appears to be that of bicarbonate (HCO_3) formation, as evidenced its characteristic δ(OH) peak at 1216 cm^{-1} (v_5) and its corresponding ν_a(OCO) and ν_s(OCO) peaks at 1599 (v_1) and 1394 cm^{-1} (v_3) respectively.[89] As for their presence on CeO_2, this signifies

14: Using the higher gas concentrations, 1 vol.% CO_2 and 4 vol.% H_2, like the previous high concentration measurement on Rh/CeO_2, shown in Figure 4.11.

Table 4.2: Assignments of the observed vibrations by DRIFTS of the adsorbates on CeO_2 during CO_2 adsorption.

Species	$\tilde{\nu}$ [cm^{-1}]	Ref.
HCO_3		
ν_a(OCO)	1599	[89]
ν_s(OCO)	1394	[89]
δ(OH)	1216	[89]

15: Or, of course, perhaps another metal which can provide a hydrogen spill-over to the support.

that the surface is at least partially hydroxylated even during the CO_2 adsorption measurement, which is not surprising as the low temperature O_2 (5 vol.%) pre-treatment (350 °C) is expected to be inefficient for the removal of strongly chemisorbed hydroxyls. However, the Rh/CeO_2 sample was exposed to both an oxygen and hydrogen pre-treatment at 350 °C, suggesting further hydroxylation, no HCO_3 was formed. This could signify that the adsorption sites of these HCO_3 species might be blocked by the deposited Rh particles, perhaps being composed of defects or other nucleation sites. Nevertheless, the O−C−O structure seen for the case of Rh/CeO_2 does not make an appearance on pure CeO_2, signifying that the presence of Rh[15] is needed in order for it to be obtained.

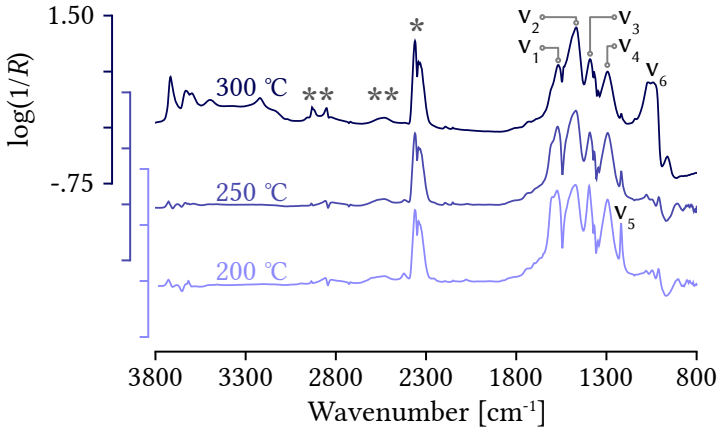

Figure 4.12: *In situ* infrared spectra collected during CO_2 adsorption (1 vol.% CO_2) on CeO_2 at 200, 250 and 300 °C. The * peaks belong to CO_2 (g). The spectra have been normalised such that the intensity of the 2360 cm^{-1} peak is equal to 1. Note the disturbed baseline for the 300 °C measurement of CeO_2. Peaks above 2400 cm^{-1} (such as **) can be attributed to artefacts, caused by a baseline shift.

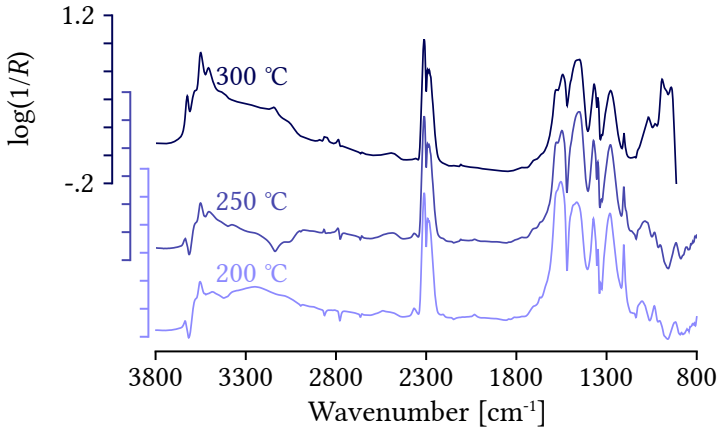

Figure 4.13: *In situ* infrared spectra collected during steady-state hydrogenation reaction conditions at increased gas concentration, i.e., 1 vol.% CO_2, 4 vol.% H_2. The spectra have been normalised such that the intensity of the 2360 cm^{-1} peak is equal to 1. The T = 250°C is cut off around 1000 cm^{-1}due to its pseudo-absorbance approaching −1.

Active species – to separate the wheat from the chaff

While providing an insight into the surface during reaction, it is difficult, if not impossible, to determine if an adsorbate is an intermediate or simply a spectator based on steady-state measurements. As such, in order to explore the possibility of these adsorbates being reaction intermediates, transient experiments with a modulation excitation approach were performed. Like the previous HE-XRD experiment, the CO_2 concentration in the gas flow was kept constant at 0.5 vol.% whereas the hydrogen concentration was modulated in a square wave fashion, alternating between 0 and 2 vol.%. However, unlike the HE-XRD, a higher sampling frequency (~2 Hz) and shorter modulation periods (τ) were employed in order to study the rapid reactions. Furthermore, both the

modulation period (τ = 30, 60, 120 s) as well as temperature (T = 200, 250, 300 °C) were varied. As an example, the case of 300 °C with a modulation period of 120 s can be seen in Figure 4.14 with the gas modulation (a), the infrared spectra (b) and the difference infrared spectra (c). As seen in Figure 4.14c, clear responses from vibrations in the carbonyl[16], carbonate[17] as well as hydroxyl and C–H[18] region were obtained. In regards to the other experiments, while the same regions showed a response, different intensities (both absolute and relative between the peaks) were obtained, for which high temperature and long periods favoured the carbonyl region in particular. Furthermore, steady-state condition was reached for several peaks at 120 s during H_2 flow. However, the hydrogenation products were never depleted during the H_2 purge steps. This is at least partially due to the dead volume of the reaction cell which prohibits a full purge of hydrogen from the gas phase during the modulation period. As such, one should take into account that the reaction is only perturbed by the modulation, not initiated and quenched.

16: 2200-1700 cm^{-1}

17: 1700-800 cm^{-1}

18: 3800-2700 cm^{-1}

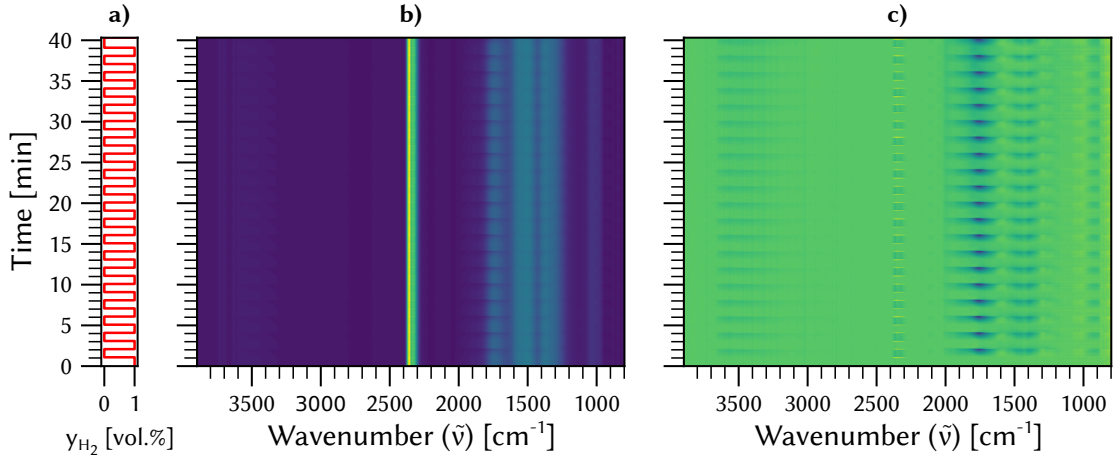

Figure 4.14: Modulation excitation spectroscopic measurement of CO_2 hydrogenation over a Rh/CeO_2 catalyst at 300 °C showing (a) the imposed H_2 concentration stimulus with period τ = 120 s, (b) collected in situ infrared difference spectra and (c) in situ infrared difference spectra where the first difference spectrum has been subtracted from each difference spectrum in the full measured range 3900-800 cm^{-1}.

In order to more easily compare the adherence of the response to the stimulus, remove static contributions as well as noise this time-resolved data was further analysed by phase sensitive detection (PSD), using a lock-in amplifier (see equation (3.14), page 11) which was integrated over several periods. The obtained phase-resolved spectra ($A^{\phi^{\mathrm{PSD}}}$) of the 2200-900 cm^{-1} region can be observed in the top rows of Figure 4.15 for modulation period 120 s (panel a), period 60 s (panel b), and period 30 s (panel c) between $0° \leq \theta^{\mathrm{PSD}} \leq 180°$[19]. Furthermore, the bottoms rows shows a composite plot in which the maximum amplitude ($A^{\phi^{\mathrm{PSD,\,max}}}$) is given at each wavenumber, given a full period of $0° \leq \theta^{\mathrm{PSD}} \leq 360°$, together with the corresponding phase delay (φ) for the most pronounced peaks, marked with bullets (•).

19: The $180° \leq \theta^{\mathrm{PSD}} \leq 360°$ interval is not included for clarity. However, it can still be visualised by taking into regard that it is simply the reflection of $0° \leq \theta^{\mathrm{PSD}} \leq 180°$ across the $\tilde{\nu}$ axis.

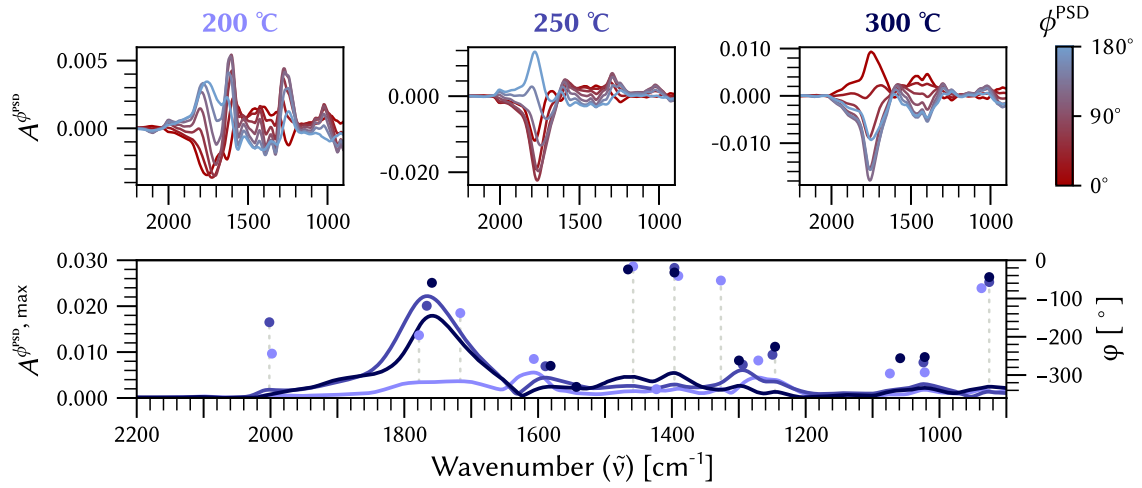

(a) Modulation period $\tau = 120$ s

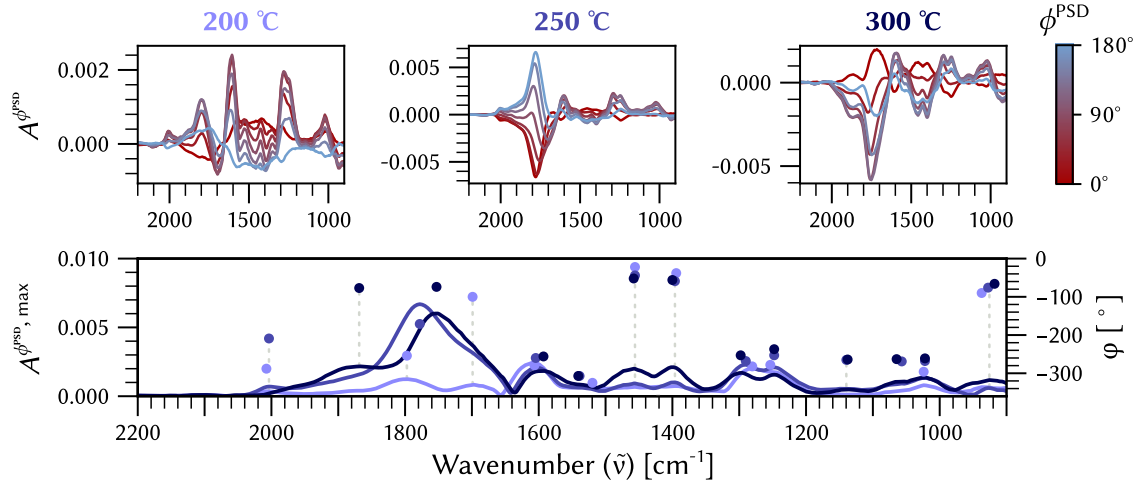

(b) Modulation period $\tau = 60$ s

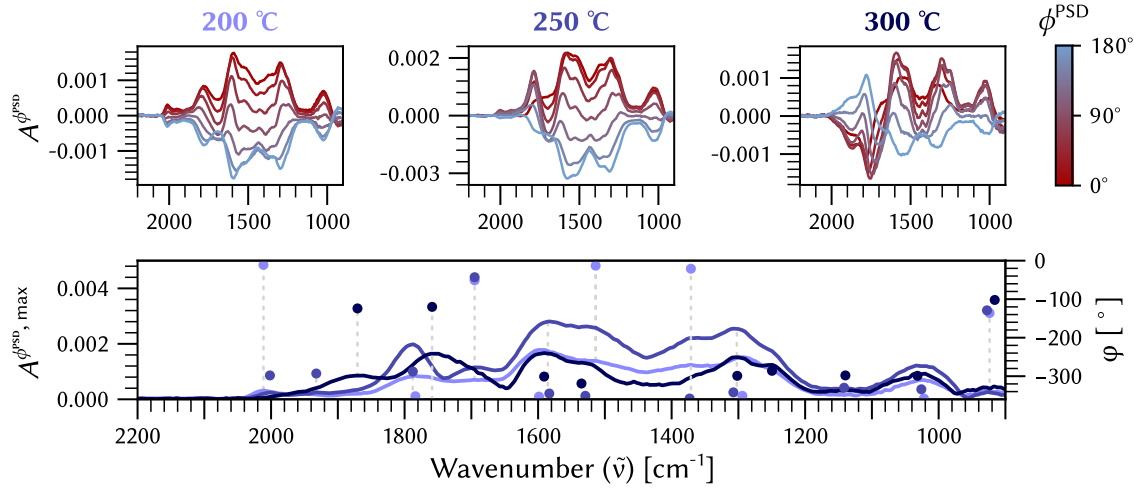

(c) Modulation period $\tau = 30$ s

Figure 4.15: Graphical representation of phase sensitive detection (PSD) analysis results for CO_2 hydrogenation over Rh/CeO_2 at 200, 250 and 300 °C and different H_2 modulation period lengths (τ) of 120, 60 and 30 s. **Top rows:** PSD plots showing amplitude ($A^{\phi^{PSD}}$) versus wavenumber for demodulated spectra between $0° \leq \theta^{PSD} \leq 180°$. **Bottom rows:** Composite plots showing maximum amplitude ($A^{\phi^{PSD, max}}$) at each wavenumber in the period of $0° \leq \theta^{PSD} \leq 360°$ (**—**) together with the phase delay (φ) of the peaks (•) and visual guides (**- - -**).

Carbonyls While minor peaks such as m-CO at 2000 cm^{-1} are seen, it is the previously assigned $\nu(C{=}O)_{Rh\text{-}CeO_2}$ vibration, from steady-state measurements, that is the most prominent peak in the MES-PSD results, given $\tau \geq 60$ s and $T \geq 250$ °C. However, while appearing as a single peak during steady-state, the MES-PSD results show that it consists of at least two separate peaks approximately located at 1700 and 1800 cm^{-1}. This is most noticeable in the $\phi^{PSD,\,max}(\tilde{\nu}, T = 200\ °C, \tau = 60\ s)$ spectrum (Figure 4.15b). Furthermore, it is unlikely that these vibrations belong to the same molecule as they do not share a phase delay (i.e. they are not formed at the same time). Out of these, the peak at 1700 cm^{-1} is expected to correspond to the previously assigned $\nu(C{=}O)_{Rh\text{-}CeO_2}$ vibration. As for the 1800 cm^{-1}, its low wavenumber makes it unlikely to correspond to a bridged CO (br-CO) and is instead likely to correspond to CO in a hollow or hollow-like site (h-CO).[90,94] While this convoluted peak is primarily located close to the 1800 cm^{-1} peak, it shifts towards lower wavenumbers with increasing temperature. While a shift of the h-CO peak towards lower wavenumbers could be due to changes to its surrounding environment, perhaps a larger contributing factor is the increase of the CO_{RhCeO_2} to h-CO ratio. Furthermore, the intensity drop of these carbonyls, compared to other peaks in the spectra, at 300 °C coincides with the formation of bridged CO (br-CO, 1875 cm^{-1}). Although this decrease in h-CO could correspond to a potential increase in consumption rate of the hydrogenation reaction, it may also be due to a increase in desorption rate (initiating CO (g) formation) or a change in coordination to br-CO due to restructuring of the Rh surface. As for the relation between CO_{RhCeO_2} and h-CO, as CO_{RhCeO_2} the lower phase delay of CO_{RhCeO_2} opens up several different possibilities in regards reaction mechanisms. As an example, these carbonyls might be dependent on each other such as CO migration from the Rh-CeO_2 site to the extended Rh surface. As such, while the Rh surface alone should be able to dissociate oxygen from CO_2, the introduction of this new active site with faster kinetics could be linked to the promotional effect of CeO_2 to Rh. However, one need to take into account that CO_{RhCeO_2} and h-CO do not share adsorption site and possibly not active site either. Factors such as ratio of adsorption sites that participate in the reaction contra only facilitate migration as well as competition with other species in regards to surface coverage will have an effect. As such, this needs to be further explored in order to support or disregard this idea.

Carbonates and formates While formates are present on the catalyst according to the previous XPS study, and the O−C−O vibrations at 1550 and 1300 cm^{-1} as well as C−H vibrations at 2950 and 2850 cm^{-1} seen in Figure 4.15 and 4.16 could in part be attributed them,[93] they do not exhibit a markedly presence on the surface nor a strong response to the hydrogen stimulus. However, some minor C−H responses seem to be present, but this might simply be due to experimental fluctuations, such as disturbances to the total flow during a gas switch, and as such it is possible that this response does not originate from a participation in the methanation reaction.

Carbonates, which often are too stable to participate in hydrogenation do show a response to the hydrogen stimulus. One such carbonate is the b-CO_3 which was previously seen in the steady-state measurement.

Table 4.3: Infrared peak assignments for the transient experiments in the 3000-2800, 2100-1700 and 1700-800 cm^{-1} region. The wavenumber values are approximated (±10 cm^{-1}) due to fluctuations during the time series and between the different experiments.

Species	$\tilde{\nu}$ [cm^{-1}]	Ref.
ν(C=O)		
$CO_{Rh\text{-}CeO_2}$	1700	[88]
h-CO	1800	[90]
br-CO	1875	[86]
m-CO	2010	[86]
p-CO_3		
ν_a(OCO)	1460	[91]
ν_s(OCO)	1390	[91]
b-CO_3		
ν_a(OCO)	1590	[92]
ν_s(OCO)	1280	[92]
b-HCOO		
ν_a(OCO)	1550	[93]
ν_s(OCO)	1300	[93]
ν(CH)	2850	[93]
δ(CH)*	2950	[93]

* In actuality a combination band of δ(CH) and ν_{as}(OCO).

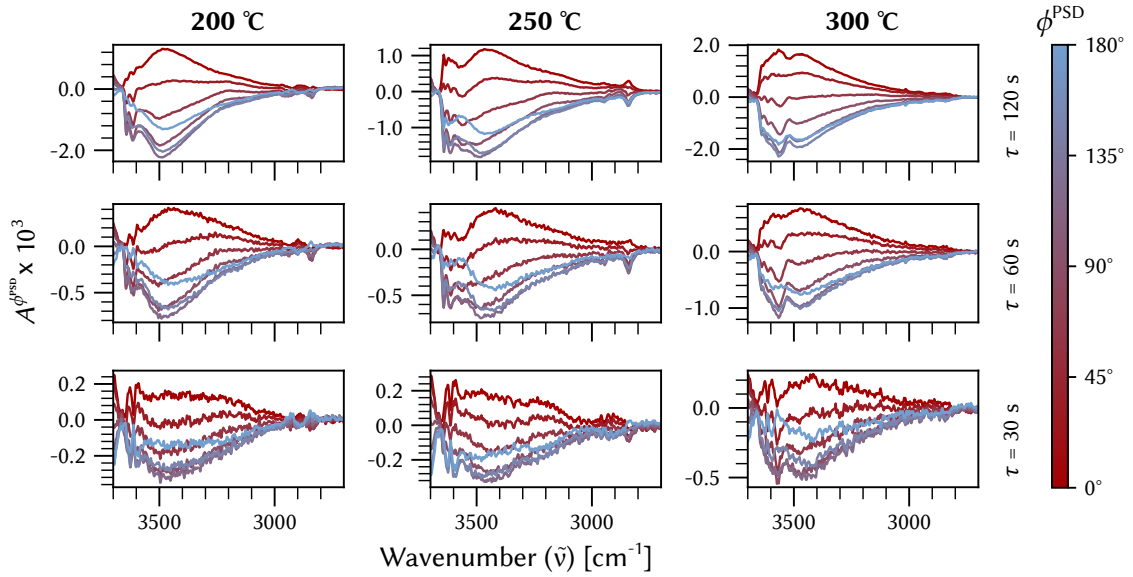

Figure 4.16: The phase resolved spectra in the region of 3700-2600 cm^{-1} of all MES-DRIFTS experiments. Peaks corresponding to C−H vibrations can be seen around 2950 (δ(CH)) and 2850 cm^{-1} (ν(CH)).

The b-CO_3 showed a huge phase delay to the modulation ($|\varphi| > 180°$), signifying a consumption during hydrogen flow rather than production, as one would expect. However, another pair of vibrations are seen in the O−C−O region, those of 1460 and 1390 cm^{-1}, who instead show a minute phase delay. One would therefore expect these to correspond to hydrogenation products, such as perhaps an inorganic carboxylate. However, the low ν_{a-s} split as well as the low wavenumber of the peaks makes this doubtful and they instead more likely correspond to polydentate carbonates.[20][89,91] As the ceria surface reduces and restructures during the H_2 step, a p-CO_3 configuration might be more favourable for CO_2 adsorption rather than the previous b-CO_3 in the oxidised state. As such, the activity of these carbonates might therefore not be linked to the methanation reaction but is instead a response to the changes in the state of ceria. To gain an insight into the formation of p-CO_3, the phase delay of the carbonates was compared. By adjusting the phase delay of b-CO_3 with half a period,[21] it is revealed that p-CO_3 has a shorter phase delay (-30°) and its formation should therefore be an earlier event than the b-CO_3 consumption. As such, the primary mode of formation for p-CO_3 should therefore be CO_2 adsorption rather than re-configuration of b-CO_3.

20: More specifically, highly symmetrical, most likely planar, polydentate carbonate. Polydentates of a more asymmetrical configuration are expected to have a larger ν_{a-s} split with a ν_a(OCO) around 1500 cm^{-1}.[89] Monodentate carbonates may also exhibit these vibrations, but this explanation was rejected by their lower thermal stability.

21: φ(b-CO_3) + 180° ≈ - 80°

A change of modulant

As the system's response to a stimulus is related to its dependence of said stimulant, one may gauge its dependence on different parameters by changing the modulant. As such, this H_2-MES study was followed up by a CO_2-MES study. Furthermore, the gas concentrations were doubled[22] as to increase the adsorbate coverage and thus the intensity of the response.

As to establish a reference, the pure CeO_2 was studied by both CO_2 and H_2 modulation at 300 °C and τ =120 s. The resulting phase spectra of these experiments may be seen in Figure 4.17. In regards to the CO_2 modulation,

22: i.e. the flow consisted of 1 vol.% CO_2 and 4 vol.% CO_2. As a consequence of this, the flow was also reduced from 200 ml_n min^{-1} to 125 ml_n min^{-1} in order to achieve these concentrations. However, while this does increase the impact from the dead volume of the cell, the increased error was deemed acceptable.

only adsorption-desorption of the carbonate species could be seen, but for the case of H_2 modulation it was seen that only some carbonate peaks showed a dependence, namely those corresponding to HCO_3. Furthermore, in phase responses of peaks corresponding to bending vibrations of H−O−H and O−H could be observed.[95,96] Nevertheless, the O−C−O peaks shown to be active for Rh/CeO_2 did not show a significant prominence, signifying that these are not inherent to the CeO_2 but instead require the presence of Rh.

Similar to the H_2-MES experiments, the different CO species showed a positive dependence to the CO_2 stimulation, as seen in Figure 4.18 as well as b-CO_3. However, unlike the case of H_2 stimulation, the central peaks attributed to p-CO_3 only show a minor appearance in the phase spectra. As for the cause of this, it is likely due to the catalyst being in a near constant oxidation state during CO_2 modulation, as suggested by the XRD study which displayed a rapid reduction followed by a slow re-oxidation. Given this, the p-CO_3 therefore only seem to have a dependence on the oxidation state of the CeO_2 rather than the reaction and thus does not show a dependence of this CO_2 modulation. Consequently, one may then regard this p-CO_3 as simply a spectator to the methanation reaction. However, caution must be taken as kinetics might play a role here. Given that it is primarily adsorbates related to rate controlling steps of the reaction that can be observed, it could also be that this lack of response from the p-CO_3 is due to its reaction step having a high H_2 dependence while that of CO_2 is low. However, as this p-CO_3 is expected to belong to an initial reaction step[23] if any, the likelihood of its response being lost due to lack of kinetic limitations is poor.

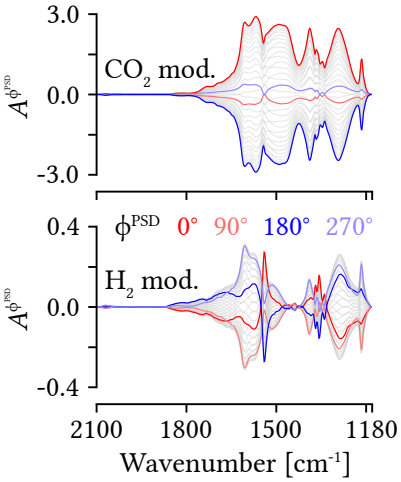

Figure 4.17: Phase domain spectra of the CO_2 and H_2 modulated experiments on CeO_2 at 300 °C.

23: The only likely reactant prior to this would be other carbonates, of which b-CO_3 is the only one which has been seen. In the phase analysis of the H_2 modulation study, it was shown that the formation of p-CO_3 by reconfiguration of b-CO_3 is unlikely. However, one may argue that this only showed that it was not the primary mode of p-CO_3 formation during H_2 modulation as the redox contribution was greater, and that this reconfiguration still may happen.

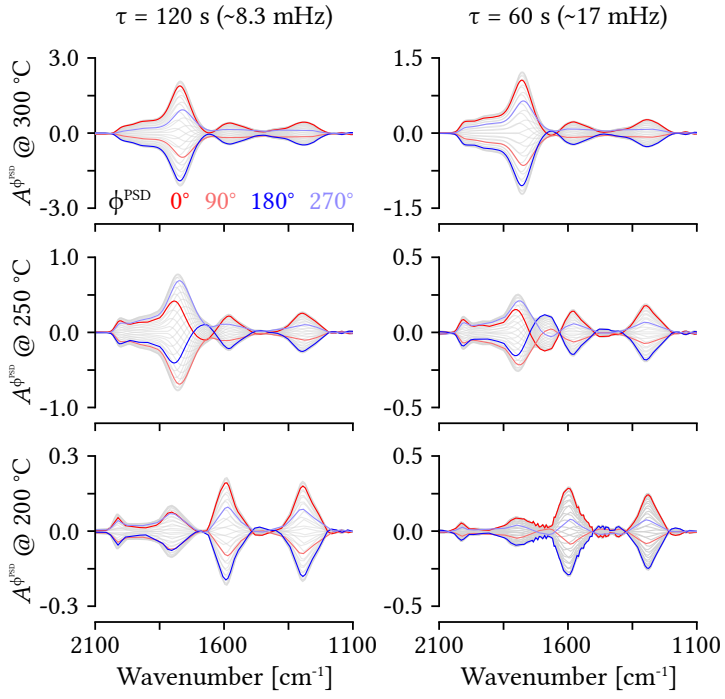

Figure 4.18: Phase domain spectra of the CO_2 modulated methanation reaction on the Rh/CeO_2 catalyst at 200, 250 and 300 °C (row) and modulation periods of 120 and 60 s (column). The step length of the $A^{\phi PSD}$ spectra is 10°.

Reaction mechanisms – formulating an idea

While a multitude of different reaction pathways for CO_2 methanation over supported metal catalysts could be theorised, only a few pathways have shown a likelihood. Of these, it is primarily the formate and carbon monoxide routes, named after their primary reaction intermediates, which have been observed experimentally.

During reaction conditions, while a portion of the rhodium is oxidised its surface is expected to be reduced whereas both the bulk and surface of ceria adopt a partially reduced structure. A number of active species in the form of carbonyls, carbonates and formates could be seen. These carbonyls were active even at low temperatures where CO (g) formation has not been observed for Rh/CeO_2. As such, one might expect that the methanation on Rh/CeO_2 follows a carbon monoxide pathway. However, some activity was also observed from formate. While not excluding the carbon monoxide pathway, it does suggest that several pathways might be involved and perhaps interact with each other, by reactions such as $HCOO \rightleftharpoons CO + OH$.

The Ce^{4+}/Ce^{3+} cycling of CeO_2 could be a contributing factor in the promotion of CeO_2 for both methanation as well as rWGS. As was seen, CO formation at the Rh-CeO_2 interface as well as surface carbonates responded to the hydrogen stimulus. A potential mechanism could be the activation of CO_2 by an oxygen vacancy on the CeO_2 surface which subsequently is hydrogenated by H_2 spill-over from the Rh metal. A similar mechanism has been proposed for other catalysts,[97] in which the oxygen vacancy is formed and healed in the reaction cycle. Similar behaviour was observed in the HE-XRD results, in which CeO_2 was partially re-oxidised during when H_2 was removed from the gas stream.

While leaving gaps for further exploration, the results of this work have provided an insight into the mechanisms behind the reaction pathway of CO_2 methanation over Rh/CeO_2.

The inhibiting effect of water on methane oxidation

5

Instead of studying carbon dioxide into methane like in paper I, II, III and IV, paper IV instead focused on an opposite path, that of methane oxidation. As such, the focus of the study was the relation between catalyst material behaviour and activity (an *operando* study) and their correlation to the inhibiting effect of water. More specifically, the impact water has on the reaction as while enjoying numerous studies for the dry state, the knowledge for mechanisms of palladium based methane oxidation catalysts in wet conditions is lacking. Some important findings were the shift of the fast Mars-van Krevelen mechanism to the slower Langmuir-Hinshelwood, due to hydroxyl build up on PdO, and the inhibition of the rim sites of the particle by a hydroxyl build up on the support.

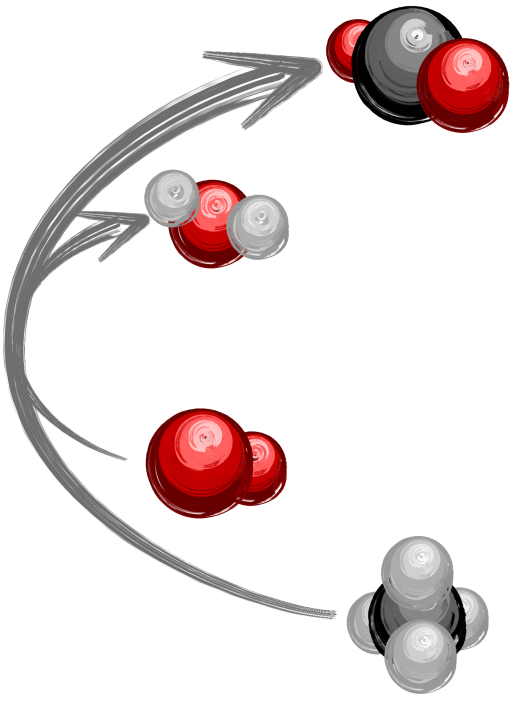

5.1 The cases of hydrophilic and hydrophobic supports

In order to gain an understanding of the nature of the inhibiting effect of water on catalytic methane oxidation over palladium-based catalysts, two kinds of catalyst formulations were made. One with palladium deposited on a hydrophilic support (Al_2O_3) and another one where instead a hydrophobic material (ZSM-5, SiO_2/Al_2O_3 = 2000) was used as support. As in previous works, palladium dispersion has been shown to be an important parameter, not least due to different properties of active sites located at the rim and on the extended surface of the particles, each type of catalyst was prepared with both high and low palladium dispersion. Palladium particle size and area, palladium dispersion and number of Pd sites for these samples were determined by CO chemisorption. Further catalytic activity was tested with flow reactor measurements, and the influence of water on catalyst surface and palladium chemical state was measured by DRIFTS and XAS, respectively.[1]

1: These methods of this study were previously described in the Sections: Catalyst preparation (p. 7), Selective probing by adsorption: Chemisorption (p. 9), Probing catalyst adsorbates by infrared spectroscopy (p. 16) and Oxidation state: X-ray absorption spectroscopy (p. 14) respectively.

Catalyst morphology and adsorption sites

Two samples each of Pd/γ-Al_2O_3 and Pd/ZSM-5 were prepared using synthesis methods that give either small or large Pd particles, or in other words high and low Pd dispersion, for each of the metal-support combinations. The catalyst morphology, i.e., Pd particle size and shape, and adsorption sites were characterised by CO chemisorption and the results are summarised in Table 5.1. In order to accomplish this, the F_s parameter[2] had to be determined. As such, the CO chemisorption was characterised further by the use of *in situ* DRIFTS, see Figure 5.1. As can be seen the carbonyls of these spectra are heavily convoluted and thus a deconvolution using Voigt profile fitting was employed, resulting in individual profiles of the different carbonyl configurations. By approximating these vibrations as having equivalent extinction coefficients, the peaks were integrated, normalised with a weight factor corresponding to number of sites for the specific vibrations, summarised and averaged.

2: The stoichiometric factor of the average number of sites occupied by the CO molecules. The importance of this parameter is presented in the section Selective probing by adsorption: Chemisorption (p. 9).

Table 5.1: Samples of the water inhibition study for methane oxidation. A_{Pd} is the exposed surface area of Pd, γ_{Pd} is the dispersion of Pd on the support and d_i is the mean particle size (i = Pd, PdO). This calculated data set is based on the CO chemisorption experiments.

Sample name	Components	w_{Pd} [wt.%]	S [$m^2\ g^{-1}$]	$V_{Chem.}$ [$\mu mol\ g^{-1}$]	F_s	A_{Pd} [$m^2\ g^{-1}$]	γ_{Pd} [%]	d_{Pd} [nm]	d_{PdO} [nm]
$PdAl_{D57\%}$	Pd/γ-Al_2O_3	1.7 ± 0.1	142.0 ± 0.3	43.0 ± 0.5	2.1	4.3	57	2.0	-
$PdAl_{D14\%}$	Pd/γ-Al_2O_3	1.8 ± 0.1	131.0 ± 0.4	11.0 ± 0.2	2.2	1.1	14	8.0	18
$PdZ_{D21\%}$	Pd/ZSM-5	1.8 ± 0.1	387.0 ± 0.7	18.0 ± 0.3	2.0	1.7	21	5.4	-
$PdZ_{D5.2\%}$	Pd/ZSM-5	1.7 ± 0.1	368.0 ± 0.7	4.1 ± 0.3	2.0	0.39	5.2	22	37

To validate the particle size estimation by CO chemisorption, TEM imaging was also employed as can be seen in Figure 5.1. The figure shows images in the form of example images together with determined particle size distributions of the measured PdO.[3] While supporting the chemisorption measurements, the TEM measurements furthermore provide an insight into the size distribution for the samples, showing a larger distribution of the samples with low dispersity.

3: Whose average is given in Table 5.1.

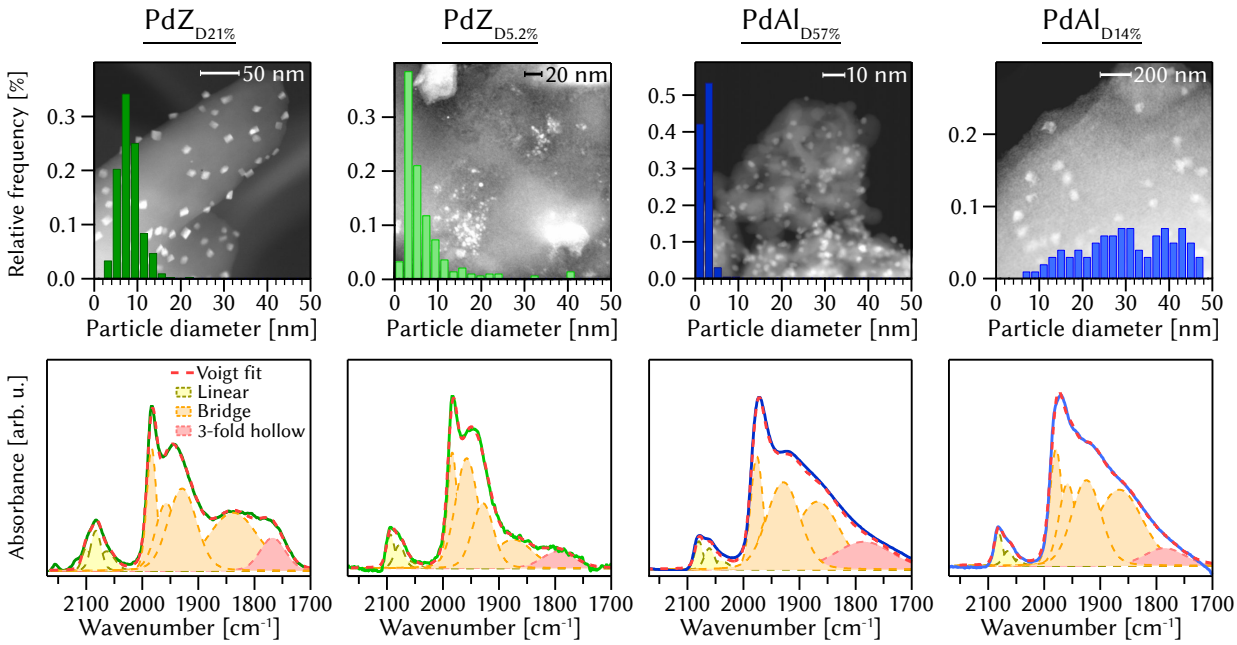

Figure 5.1: Upper row: Transmission electron microscopy images for the palladium samples (in oxidised state, PdO) together with an overlaid plot of the particle size distribution. **Lower row:** The IR spectra of the samples after CO chemisorption. The samples TEM and IR are ordered columnwise.

Linking activity to changes in the catalyst

The observed activity of the catalysts at 400 °C with a feed of 0.1 vol.% CH_4 and 2 vol.% O_2 is presented in Figure 5.2 as TOF[4] against time. In this plot, one finds an initial period with high catalytic activity when a dry gas is fed, which is followed by a drop upon the introduction of 10 vol% H_2O into the gas feed and, finally, a period with increased activity when dry gas is again introduced. While showing a higher TOF than their counterpart, the sample with low dispersion exhibits a lower total conversion. As such, this could suggest that a larger portion of highly active surfaces may be present on the larger particles, potentially facilitated by disproportional growth of different facets. However, although interesting, this is not the scope of this study and is thus not discussed more here. Moving on, the sharp drop in activity upon the introduction of water into the gas feed suggests a competitive adsorption between reactants and the water, which hampers the reaction rate. Later on, when water is removed from the gas feed, the PdZ samples regain their activity whereas the PdAl samples suffer from a irreversible deactivation[5]. In order to correlate this change in activity to the influence of water, *in situ* DRIFTS was performed in which the samples were, similar to the flow reactor measurements, exposed to a dry and humid gas feed (2 vol.% H_2O at 300 °C). As seen in Figure 5.3, while initially during the dry feed having a presence of hydroxyl[6] and potentially also some surface condensed water, its content dramatically increased on PdAl$_{D57\%}$ during the water step[7] and do not subside to its original level after the removal of water from the feed. Interestingly, this further suggests that at these conditions stable and inhibiting hydroxyl groups could be formed by water adsorption, which could not be formed from hydrogen spillover from the Pd surface to the support. As for PdZ$_{D21\%}$, little to no water or hydroxyl group were shown to be present on the sample. The cause for this could be attributed

4: TOF, Turn Over Frequency, is the average rate per reaction site. While theoretically a suitable descriptor for the activity of a catalyst, in practice it may provide a false impression of accuracy simply due to a lack of insight into what is constituting the active site of the catalyst. In the presented result, the whole surface of the Pd particle is treated as active and was thus used as the normalisation factor (using the chemisorption data to obtain number of Pd sites). In reality, certain regions of this surface might provide a much higher activity than the rest while other regions might even be inactive. As such, do not regard this presented TOF as true but simply an attempt to more accurately normalise the activity.

5: While irreversible in the case of continuous flow during and following this measurement, the activity could be regained by a high temperature treatment in dry conditions. This is not showcased in the presented data set.

6: See Table 5.2 for the peak assignments.

7: Do take note that although parts of the hydroxyl and water uptake seen during this step could be contributed to the decrease in activity, a large portion of this increase is likely originating from sites on the extended surface which do not participate in the reaction and are thus simply spectators. However, one could also envision these extended sites as acting as a hydroxyl reservoir, supplying hydroxyl to the active sites by mechanisms such as surface diffusion.

to the hydrophilicity and hydrophobicity for the $PdAl_{D57\%}$ and $PdZ_{D21\%}$ sample respectively. As such, it is perhaps primarily the rim sites of palladium that cause the irreversible drop in activity for the alumina samples, as they are subject to the inhibiting hydroxyls from the support. Due to the lack of a significant hydroxyl buildup on the ZSM-5 samples, these ones are not subject to this irreversible deactivating process[8].

8: However, as they displayed a drop in activity they still suffer from water inhibition, albeit this inhibition is likely predominately on the extended PdO surface rather than the rim sites.

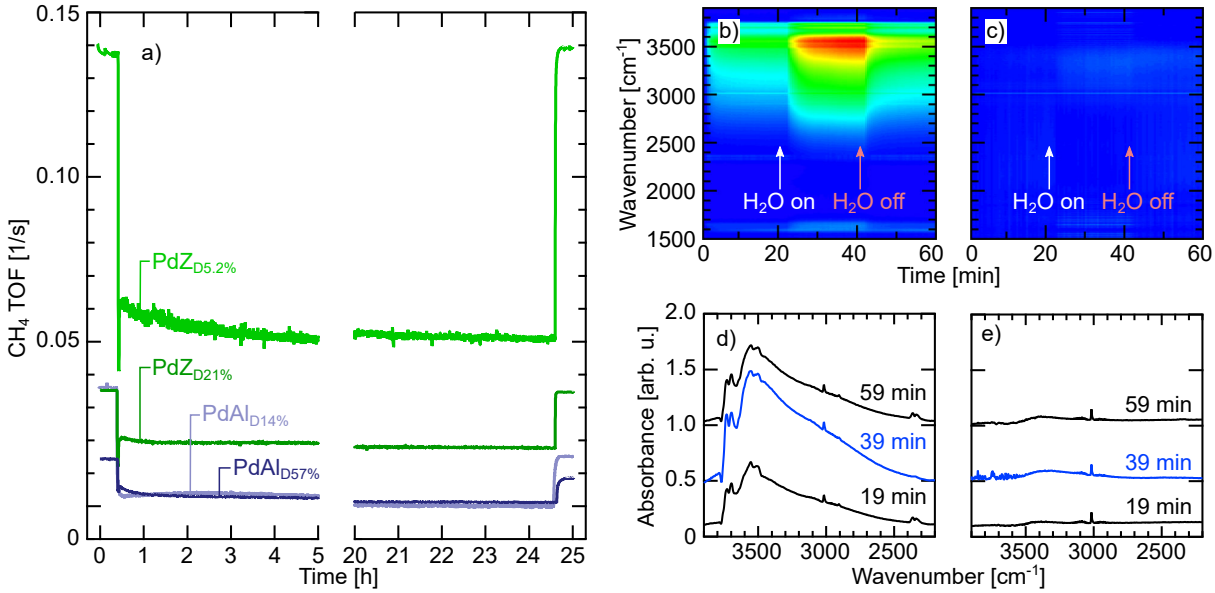

Figure 5.2: (a) The turn-over frequency of CH_4 oxidation against time with a primary feed of 0.1 vol.% CH_4 and 2vol.% O_2 in He at 400 °C. The time period consists of three regions, an initially dry one (0-0.5 h) followed by the introduction of 10 vol.% H_2O in the feed (0.5-24.5 h) and the subsequent removal of H_2O from the feed (24.5-25 h). **(b, c)** Time-resolved contour plot of DRIFTS spectra of $PdAl_{D57\%}$ and $PdZ_{D21\%}$ respectively, during an inital period with a dry feed, followed by a water step and ending with a dry feed once more. Selected spectra for the samples at different points in time are given in **(d)** and **(e)** respectively.

While giving an insight into the mechanistic behaviour of the water inhibition, parameters such as the oxidation state of Pd, during these conditions remained constant. As such, these flow reactor and infrared measurements were further supplemented by an *operando* ED-XAS[9] study in which an MES approach was utilised, consisting of O_2 pulses to a constant (dry and wet) CH_4 stream and H_2O pulses to a constant lean feed[10] . For these experiments, the white line intensity (WLI) was used as descriptor for the changes of the palladium oxidation state[11] and it was recorded simultaneously as the reaction activity (expressed as TOF). A general behaviour for the different catalysts in dry conditions is the initial large increase in activity and oxidation, which could be explained by the WLI[12] as a rapid formation of surface oxide, followed by a slower bulk oxidation. Removal of O_2 from the gas feed resulted in a swift decrease in WLI and activity as the sample becomes reduced by the dissociation of CH_4. However, while the activities and oxidation states return during the O_2 cycling in dry conditions, in regards to the WLI only the $PdAl_{D57\%}$ sample shows the same behaviour in wet conditions, while the other samples display a slower oxidation and lack the rapid reduction. Indeed, not until after the second pulse, an oxidation state comparable to the one seen for dry conditions is achieved for these catalysts. Furthermore, a near constant oxidation state is maintained for the water pulsing experiment while the activity of the catalysts alternated between a high and low state. As such, the water not only blocks the oxidised sites, preventing them from being reduced, but also inhibits the oxidation of the remaining

9: Energy-Dispersive X-ray Absorption Spectroscopy, see Oxidation state: X-ray absorption spectroscopy (p. 14)

10: 1.5 vol.% O_2, 0.1 vol.% CH_4 and 1 vol.% H_2O, diluted in He. F_{tot} = 75 ml_n min^{-1}, T = 360 °C

11: Quantification of the oxidation state was not performed, the focus is on the change itself rather than its magnitude.

12: White Line Intensity

metal[13]. In regards to the mechanistic description of this, previous studies by Cullis *et al.* has proposed a hydroxylation of the active PdO surface into one composed of inactive $Pd(OH)_2$, preventing the Mars-van Krevelen mechanism of CH_4 oxidation to take place as oxygen surface lattice atoms are not available.[45] While mechanistically sound, the low stability of $Pd(OH)_2$[14] casts some doubt on it. Although the XAS study by Barret *et al.* at higher temperatures shows a potential existence of $Pd(OH)_2$, it is likely limited to the surface, making it difficult to distinguish from surface hydroxyl species.[98] As such, instead of forming an inactive $Pd(OH)_2$ phase, the inhibition could be explained by surface hydroxylation of the PdO particles. This idea would be further supported by the work of van den Bossche *et al.* and Li *et al.* who independently show by DFT that water may adsorb as hydroxyls on the PdO(101) surface and by XPS a surface hydroxyl buildup (without $Pd(OH)_2$) on a Pd foil after the addition of water (at 350-600 °C).[46,99]

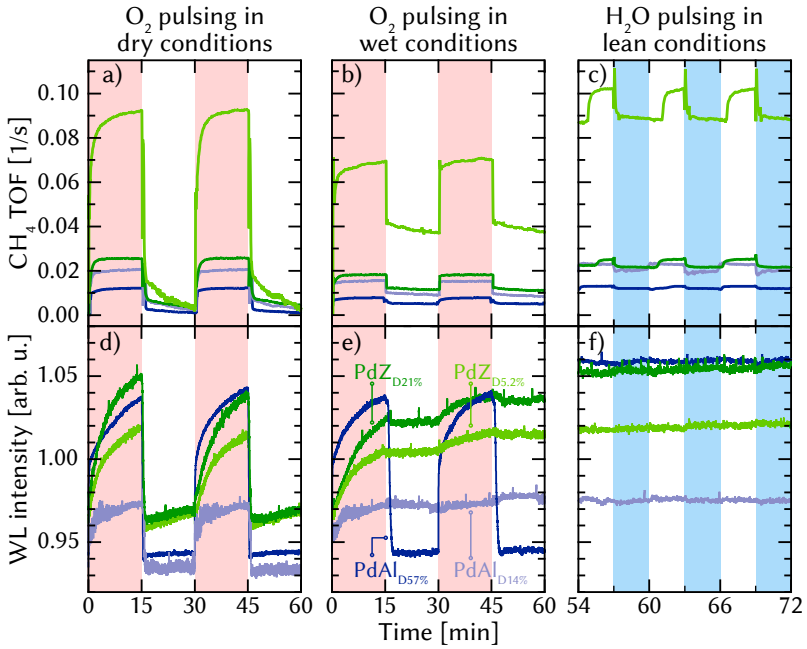

Figure 5.3: *Operando* ED-XAS measurements of Pd K-edge WLI for the $PdZ_{D21\%}$, $PdZ_{D5.2\%}$, $PdAl_{D57\%}$ and $PdZ_{D14\%}$ samples during O_2 pulsing (with constant CH_4 flow) in dry condition, a and d, as well as wet condition, b and e. In addition to this, the effect of water pulsing to a constant stream of O_2+CH_4 is shown in c and f.

13: Regarding the inhibition of oxidation, this is perchance coupled with a potential decrease in neighbouring sites which would allow O_2 to dissociate on the metal surface and the decreased reaction rate.

14: However, while $Pd(OH)_2$ has a decomposition temperature of 250 °C (well below that of reaction conditions), the high H_2O content could potentially shift the equilibrium such that it may still be present on the surface under the experimental conditions, albeit supposedly at insignificant amounts.

Table 5.2: Assignments of the hydroxyl groups seen for $PdAl_{D57\%}$, given for the wavenumber ($\tilde{\nu}$), at which surface facet the aluminium its adsorbed to is located and that aluminium's coordination (N).

$\tilde{\nu}$ [cm^{-1}]	Facet	N	Ref.
Terminal			
3770	(100)	8	[100, 101]
Bridged			
3732	(111)	8	[100, 101]
3694	(110)	8	[101–103]
Triple-bridged			
3555	(100)	8	[100, 101]
Pertubed terminal			
3501			[104, 105]

Condensing the results

The methane oxidation by catalysts based off palladium on alumina and ZSM-5 was seen to be inhibited by water. The hydrophilic Pd/Al_2O_3 showed an irreversible drop in activity under these reaction conditions if exposed to water while the hydrophobic Pd/ZSM-5 catalysts returned to what appeared to be the same kinetics upon removal of water from the gas stream. This was correlated to a hampered redox behaviour of the catalysts, as seen by XAS, as well as hydroxyl build-up, as seen by DRIFTS. Based on this, it is proposed that the deactivation process involved a blockage of the PdO sites needed for the Mars-Van Krevelen mechanism by hydroxyl accumulation. Furthermore, the irreversible activity loss for the alumina based catalyst is supposedly linked the rim sites of the palladium particles and that it is hydroxyls from the support which suppress these sites.

Conclusions and outlook 6

6.1 Sketching out pathways

On methanation on rhodium catalysts

In order to relate changes of structure, oxidation state and adsorbates to potential reaction mechanisms of CO_2 methanation on rhodium based metal-metal oxide catalysts, Rh/Al_2O_3, Rh/SiO_2 and Rh/CeO_2 were studied. Regarding the Rh/Al_2O_3 and Rh/SiO_2 catalysts, *in situ* HE-XRD, XAS and DRIFTS were employed to study their reaction dynamics. It was shown that the deposited Rh particles adopted a partially oxidised state and that this formed RhO_x was active during the reaction due to a CO_2 dissociation occurring on the metal surface.[1] Based on these findings, the reaction is expected to follow a carbon monoxide based pathway, such as possibly the carbide pathway,[2] on these catalysts. Furthermore, as only CO appeared to accumulate on the catalyst surface, without any noticeable amount of vibrations corresponding to C−H bonds, the dissociation of CO into C or hydrogenation of CO is expected to be a rate limiting step of the reaction.

While Rh/Al_2O_3 and Rh/SiO_2 displayed quite simple systems, the Rh/CeO_2 catalyst showcased a more complex one. The structural changes of the Rh/CeO_2 catalyst and its surface reactions during CO_2 methanation were studied *in situ* by HE-XRD, AP-XPS and DRIFTS. It was revealed that CeO_2 takes an active role, cycling between Ce^{4+} and Ce^{3+}. Presumably, this is due to the formation of oxygen vacancies which are further on partially healed by an intermediate involved in the reaction. Furthermore, while the rhodium was shown to be predominately in a reduced state during the reaction, a RhO_x phase was observed. This RhO_x could not be removed by reduction and is likely located at the intermediary region of Rh and CeO_2, caused by a strong metal support interaction.

The presence of active carbon monoxides on the catalyst strongly suggests that the Rh/CeO_2, like Rh/Al_2O_3 and Rh/SiO_2, follows a carbon monoxide route, possibly the carbide pathway. The Ce^{4+} and Ce^{3+} of CeO_2 affected the configuration of adsorbed carbonates, alternating between b-CO_3 and p-CO_3. While not being disproved of being involved in the methanation reaction, lacking an active response of the p-CO_3 while the CO_2 was modulated casts doubt on this idea and as such it is likely a spectator side process.

While formate could be observed by XPS, any significant amount could not be observed by DRIFTS. As such, this formate likely only constituted a minor amount and any activity it may have shown was due to an equilibrium reaction[3] rather than a support for the formate pathway being present. Furthermore, the formation of this formate could have been alleviated by CO_2 activation by the reduced CeO_2, possibly involving a short-lived bicarbonate (HCO_3) intermediate as reported for other catalysts.[27]

1: However, there was also a contribution to the oxidation by a metal-support interaction, but this is unlikely to participate in the change in oxidation state during the reaction cycle.

2: Which was presented on page 4.

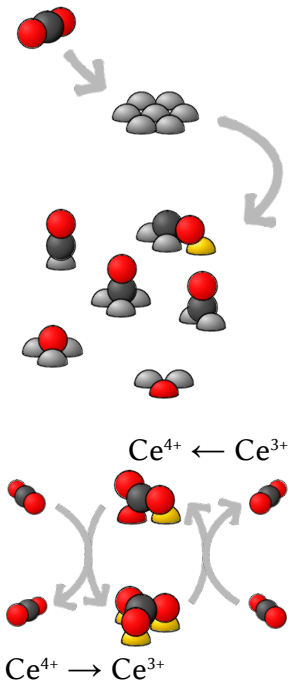

Figure 6.1: A cartoon illustrating the observed active groups during the methanation studies, with the carbonyl formation and surface oxidation (top) and the carbonate cycle (bottom).

3: Such as formate decomposition
$HCOO \rightleftharpoons CO + OH$

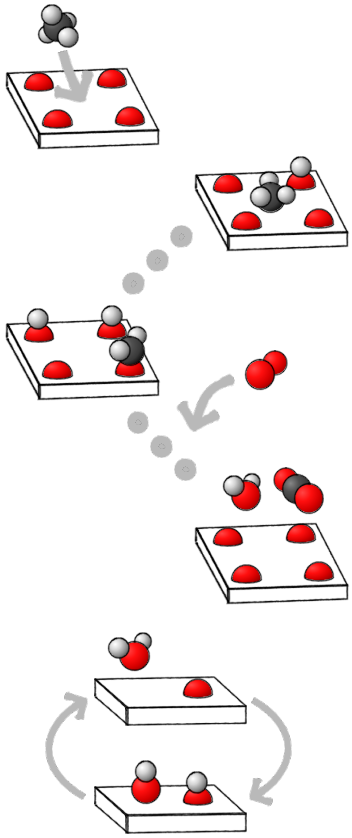

Figure 6.2: A cartoon illustrating few steps of the Mars-Van Krevelen reaction on PdO[99] (upper) and the dissociative adsorption of water which blocks the surface oxygen atoms (lower).

4: i.e. only responding to the build up of carbon monoxide on the surface, being a result of surface diffusion and reconfiguration as to lower the energy caused by the shift in coverage.

Methane oxidation during water inhibition

Catalysts used for methane oxidation such as Pd/Al_2O_3 suffer from a markedly decrease in activity if operating in gas flows with high water content. In this work, it was shown that this activity drop was correlated to an increased coverage of hydroxyl species on the surface as well as lowered ability to reduce and oxidise the sample. By comparing palladium catalysts with a high and low particle dispersion on hydrophilic and hydrophobic supports, this inhibition by water appeared to influence two different regions, a reversible occurring on the extended metal PdO/Pd surface and an irreversible at the rim sites of the particle (seen for hydrophilic support). As for the nature of mechanism of this inhibition, a potential explanation is the blockage of the active PdO sites by hydroxyl groups, prohibiting the dissociation and subsequent oxidation of CH_4 on the PdO surface, disabling the Mars-Van Krevelen mechanism at that site.

6.2 Some remaining questions and how to answer them

Are all carbonyls on rhodium equal? Two kinds of carbonyls corresponding to adsorbed carbon monoxide were observed on Rh/SiO_2 and Rh/Al_2O_3, bridged and linear, with additional ones making an appearance on Rh/CeO_2, in particular at hollow site and Rh-CeO_2 interface. While not delving deeply into their behaviour for the SiO_2 and Al_2O_3 case, CeO_2 enjoyed a deeper study. While an attempt at resolving the phases of the observed carbonyls was performed, the error margin of the study, in particular due to the dead volume of the DRIFTS cell, limits the reliable resolution of these phases. It would be of interest to determine which of these which are principal intermediates and if any of them may simply act as a buffer.[4] In particular the one at the interface as it could be related to a faster reaction step. A follow up study could therefore focus on their particle size dependence, studying the interface effect by correlation. In order to achieve this with a greater degree of control, it would be fitting to change the synthesis route. Instead of forming the particles on the support directly, these particles could be formed in solution and later on be deposited on the support. With a suitable synthesis, one could then control shape and size of the particle independently on the support effect. Furthermore, this would alleviate the comparison of different supports as particle size typically become aliased in those studies.

Could the result truly be separated from potentially irrelevant redox effects? While complementing the H_2 modulation with one by CO_2 appear to have allowed a study with significant shifts in oxidation state and one without, this is only based on the observed behaviour and extrapolation from behaviour seen during H_2 modulation. If one would truly want to be sure that the net oxidation state as well as reaction remain in steady state, this switch-on-off modulation experiment could have been complemented with a steady-state isotope transient kinetics analysis (SSITKA) in which the modulant would instead have been an isotope exchange. Indeed, with both of these studies both the steady-state

behaviour as well as the initial build up and depletion of surface species could have been studied.

Does water truly kill the Mars-Van Krevelen oxidation mechanism? While surface poisoning by hydroxyls, which in turn would prohibit the Mars-Van Krevelen mechanism as surface lattice oxygen would not be interactable, the methane oxidation still occurs. This could be due to other reaction routes such as a Langmuir-Hinshelwood mechanism with adsorbed oxygen, rather than surface lattice oxygen. Nevertheless, one would still expect some Mars-Van Krevelen to occur as there should be a competitive adsorption between the reactant and water, making the likelihood of reaction occurring low but not non-existant. In order to study this, an isotope labelled experiment could be conducted. As an example, the catalyst could be pre-oxidised with O^{17} and then covered by hydroxide by a water flow. By later on introducing the reactant gas into the feed one could study the product formation and how the isotope ratios shift between wet and dry cases.

Bibliography

[1] J. Artz, T. E. Müller, K. Thenert, J. Kleinekorte, R. Meys, A. Sternberg, A. Bardow, W. Leitner, *Chemical Reviews* **2018-01**, *118*, 434–504.

[2] W. Wang, S. Wang, X. Ma, J. Gong, *Chem. Soc. Rev.* **2011**, *40*, 3703–3727.

[3] N. Kannan, D. Vakeesan, *Renewable and Sustainable Energy Reviews* **2016**, *62*, 1092–1105.

[4] P. D. Lund, J. Lindgren, J. Mikkola, J. Salpakari, *Renewable and Sustainable Energy Reviews* **2015**, *45*, 785–807.

[5] F. Orecchini, *International Journal of Hydrogen Energy* **2006**, *31*, 1951–1954.

[6] J. Abe, A. Popoola, E. Ajenifuja, O. Popoola, *International Journal of Hydrogen Energy* **2019**, *44*, 15072–15086.

[7] A. Kirubakaran, S. Jain, R. Nema, *Renewable and Sustainable Energy Reviews* **2009**, *13*, 2430–2440.

[8] C. Villante, A. Genovese, *International Journal of Hydrogen Energy* **2012**, *37*, Hydrogen Enriched Methane, 11541–11548.

[9] V. P. Utgikar, T. Thiesen, *Technology in Society* **2005**, *27*, 315–320.

[10] H. J. Pasman, W. J. Rogers, *Journal of Loss Prevention in the Process Industries* **2010**, *23*, Papers Presented at the 2009 International Symposium of the Mary Kay O'Connor Process Safety Center, 697–704.

[11] C. San Marchi, E. Hecht, I. Ekoto, K. Groth, C. LaFleur, B. Somerday, R. Mukundan, T. Rockward, J. Keller, C. James, *International Journal of Hydrogen Energy* **2017**, *42*, Special issue on The 6th International Conference on Hydrogen Safety (ICHS 2015), 19-21 October 2015, Yokohama, Japan, 7263–7274.

[12] C. Vogt, M. Monai, G. J. Kramer, B. M. Weckhuysen, *Nature Catalysis* **2019**, *2*, 188–197.

[13] S. Verhelst, J. W. Turner, L. Sileghem, J. Vancoillie, *Progress in Energy and Combustion Science* **2019**, *70*, 43–88.

[14] S. Hänggi, P. Elbert, T. Bütler, U. Cabalzar, S. Teske, C. Bach, C. Onder, *Energy Reports* **2019**, *5*, 555–569.

[15] The Sabatier System: Producing Water on the Space Station, NASA.gov, NASA, **2011**, `https://www.nasa.gov/mission_pages/station/research/news/sabatier.html` (visited on 2020-05-17).

[16] H. Blanco, A. Faaij, *Renewable and Sustainable Energy Reviews* **2018**, *81*, 1049–1086.

[17] Understanding Global Warming Potentials, epa.gov, United States Environmental Protection Agency, **2020**, `https://www.epa.gov/ghgemissions/understanding-global-warming-potentials#Learn%5C%20why` (visited on 2021-03-11).

[18] W. J. Collins, C. P. Webber, P. M. Cox, C. Huntingford, J. Lowe, S. Sitch, S. E. Chadburn, E. Comyn-Platt, A. B. Harper, G. Hayman, T. Powell, *Environmental Research Letters* **2018-04**, *13*, 054003.

[19] A Diamond Is Forever, debeersgroup.com, De Beers Group, **2021**, `https://www.debeersgroup.com/about-us/a-diamond-is-forever` (visited on 2021-03-11).

[20] C. L. Yaws in *Yaws' Critical Property Data for Chemical Engineers and Chemists*, Knovel, **2012**.

[21] I. Chorkendorff, J. Niemantsverdriet, *Concepts of Modern Catalysis and Kinetics*, Wiley, **2017**.

[22] M. Seemann, H. Thunman in *Substitute Natural Gas from Waste*, (Eds.: M. Materazzi, P. U. Foscolo), Academic Press, **2019**, pp. 221–243.

[23] S. Rönsch, J. Schneider, S. Matthischke, M. Schlüter, M. Götz, J. Lefebvre, P. Prabhakaran, S. Bajohr, *Fuel* **2016**, *166*, 276–296.

[24] Paul Sabatier – Nobel Lecture, NobelPrize.org, Nobel Media AB, **2020**, `https://www.nobelprize.org/prizes/chemistry/1912/sabatier/lecture/` (visited on 2020-05-17).

[25] G. Varvoutis, M. Lykaki, S. Stefa, E. Papista, S. A. Carabineiro, G. E. Marnellos, M. Konsolakis, *Catalysis Communications* **2020**, *142*, 106036.

[26] M. Younas, L. Loong Kong, M. J. K. Bashir, H. Nadeem, A. Shehzad, S. Sethupathi, *Energy & Fuels* **2016**, *30*, 8815–8831.

[27] E. Baraj, S. Vagaský, T. Hlinčík, K. Ciahotný, V. Tekáč, *Chemical Papers* **2016-04**, *70*, 395–403.

[28] P. Frontera, A. Macario, M. Ferraro, P. Antonucci, *Catalysts* **2017**, *7*, 59.

[29] J. Barrientos, M. Lualdi, R. Suárez París, V. Montes, M. Boutonnet, S. Järås, *Applied Catalysis A: General* **2015**, *502*, 276–286.

[30] S. Kattel, B. Yan, Y. Yang, J. G. Chen, P. Liu, *Journal of the American Chemical Society* **2016**, *138*, PMID: 27571313, 12440–12450.

[31] J. Ren, H. Guo, J. Yang, Z. Qin, J. Lin, Z. Li, *Applied Surface Science* **2015**, *351*, 504–516.

[32] A. A. Latimer, A. R. Kulkarni, H. Aljama, J. H. Montoya, J. S. Yoo, C. Tsai, F. Abild-Pedersen, F. Studt, J. K. Nørskov, *Nature Materials* **2017-02**, *16*, 225–229.

[33] R. Gholami, M. Alyani, K. J. Smith, *Catalysts* **2015**, *5*, 561–594.

[34] J. Nilsson, P.-A. Carlsson, N. M. Martin, E. C. Adams, G. Agostini, H. Grönbeck, M. Skoglundh, *Journal of Catalysis* **2017**, *356*, 237–245.

[35] J. Nilsson, P.-A. Carlsson, N. M. Martin, P. Velin, D. M. Meira, H. Grönbeck, M. Skoglundh, *Catalysis Communications* **2018**, *109*, 24–27.

[36] S. Fouladvand, S. Schernich, J. Libuda, H. Grönbeck, T. Pingel, E. Olsson, M. Skoglundh, P.-A. Carlsson, *Topics in Catalysis* **2013**, *56*, 410–415.

[37] J. Nilsson, P.-A. Carlsson, S. Fouladvand, N. M. Martin, J. Gustafson, M. A. Newton, E. Lundgren, H. Grönbeck, M. Skoglundh, *ACS Catalysis* **2015**, *5*, 2481–2489.

[38] P. Velin, M. Ek, M. Skoglundh, A. Schaefer, A. Raj, D. Thompsett, G. Smedler, P.-A. Carlsson, *The Journal of Physical Chemistry C* **2019**, *123*, 25724–25737.

[39] P. Velin, C.-R. Florén, M. Skoglundh, A. Raj, D. Thompsett, G. Smedler, P.-A. Carlsson, *Catalysis Science & Technology* **2020**, *10*, 5460–5469.

[40] D. Jiang, K. Khivantsev, Y. Wang, *ACS Catalysis* **2020**, *10*, 14304–14314.

[41] L. He, Y. Fan, J. Bellettre, J. Yue, L. Luo, *Renewable and Sustainable Energy Reviews* **2020**, *119*, 109589.

[42] N. Kamiuchi, K. Eguchi in *Catalysis for Alternative Energy Generation*, (Eds.: L. Guczi, A. Erdôhelyi), Springer New York, New York, NY, **2012**, pp. 305–327.

[43] M. Trueba, S. P. Trasatti, *European Journal of Inorganic Chemistry* **2005**, *2005*, 3393–3403.

[44] K.-i. Fujimoto, F. H. Ribeiro, M. Avalos-Borja, E. Iglesia, *Journal of Catalysis* **1998**, *179*, 431–442.

[45] W. R. Schwartz, L. D. Pfefferle, *The Journal of Physical Chemistry C* **2012**, *116*, 8571–8578.

[46] X. Li, X. Wang, K. Roy, J. A. van Bokhoven, L. Artiglia, *ACS Catalysis* **2020**, *10*, 5783–5792.

[47] J. Thomas, W. Thomas, *Principles and Practice of Heterogeneous Catalysis*, Wiley, **2014**, p. 41.

[48] G. Ertl, H. Knözinger, J. Weitkamp, *Preparation of Solid Catalysts*, Wiley, **2008**.

[49] T. Wakihara, A. Ihara, S. Inagaki, J. Tatami, K. Sato, K. Komeya, T. Meguro, Y. Kubota, A. Nakahira, *Crystal Growth & Design* **2011**, *11*, 5153–5158.

[50] E. Marceau, X. Carrier, M. Che in *Synthesis of Solid Catalysts*, John Wiley & Sons, Ltd, **2009**, Chapter 4, pp. 59–82.

[51] M. V. Landau in *Synthesis of Solid Catalysts*, John Wiley & Sons, Ltd, **2009**, Chapter 5, pp. 83–109.

[52] S. Hermans in *Synthesis of Solid Catalysts*, John Wiley & Sons, Ltd, **2009**, Chapter 8, pp. 153–171.

[53] P. Webb, C. Orr, M. I. Corporation in *Analytical Methods in Fine Particle Technology*, Micromeritics Instrument Corporation, **1997**, Chapter 3, pp. 53–152.

[54] P. Webb, C. Orr, M. I. Corporation in *Analytical Methods in Fine Particle Technology*, Micromeritics Instrument Corporation, **1997**, Chapter 3, pp. 219–271.

[55] P. Müller, I. Hermans, *Industrial & Engineering Chemistry Research* **2017**, *56*, 1123–1136.

[56] D. Baurecht, I. Porth, U. Fringeli, *Vibrational Spectroscopy* **2002**, *30*, Papers Presented at the 1st International Conference on Advanced Vibrational Spectroscopy, Turku, Finland, August 19-24, 2001, 85–92.

[57] D. Baurecht, U. P. Fringeli, *Review of Scientific Instruments* **2001**, *72*, 3782–3792.

[58] A. Urakawa, T. Bürgi, A. Baiker, *Chemical Engineering Science* **2008**, *63*, 5TH Unsteady-State Processes in Catalysis: a Special Issue of Chemical Engineering Science, 4902–4909.

[59] The Editors of Encyclopaedia, Max Von Laue, Encyclopædia Britannica, **2020**, `https://www.britannica.com/biography/Max-von-Laue` (visited on 2021-03-08).

[60] L. Smart, E. Moore, *Solid State Chemistry: An Introduction, Fourth Edition*, CRC Press, **2016**.

[61] W. H. Bragg, W. L. Bragg, *Proceedings of the Royal Society of London. Series A Containing Papers of a Mathematical and Physical Character* **1913**, *88*, 428–438.

[62] A. M. Glazer, *A Journey into Reciprocal Space*, Morgan & Claypool Publishers, **2017**.

[63] P. Hofmann, *Solid State Physics : An Introduction*, John Wiley & Sons, Incorporated, Berlin, GERMANY, **2015**.

[64] C. Zhang, J. Gustafson, L. R. Merte, J. Evertsson, K. Norén, S. Carlson, H. Svensson, P.-A. Carlsson, *Review of Scientific Instruments* **2015**, *86*, 033112.

[65] The Editors of Encyclopaedia, Photoelectric effect, Encyclopædia Britannica, **2020**, `https://www.britannica.com/science/photoelectric-effect` (visited on 2021-03-08).

[66] O. Karslıoğlu, H. Bluhm in *Operando Research in Heterogeneous Catalysis*, (Eds.: J. Frenken, I. Groot), Springer International Publishing, Cham, **2017**, pp. 31–57.

[67] J. Watts, J. Wolstenholme, *An Introduction to Surface Analysis by XPS and AES*, Wiley, **2019**.

[68] E. Wachsman, *Solid State Ionic Devices 6 – Nano Ionics*, Electrochemical Society, **2009**, p. 256.

[69] S. Calvin, *XAFS for Everyone*, Taylor & Francis, **2013**.

[70] J. A. van Bokhoven, C. Lamberti, *X-Ray Absorption and X-Ray Emission Spectroscopy : Theory and Applications : Theory and Applications*, John Wiley & Sons, Incorporated, New York, UNITED KINGDOM, **2016**.

[71] M. Haschke, *Laboratory Micro-X-Ray Fluorescence Spectroscopy*, (Eds.: G. Ertl, H. Lüth, D. L. Mills), Springer, Cham, **2014**, pp. 1–15.

[72] P. J. Larkin in *Infrared and Raman Spectroscopy (Second Edition)*, (Ed.: P. J. Larkin), Elsevier, **2018**, pp. 7–28.

[73] P. J. Larkin in *Infrared and Raman Spectroscopy (Second Edition)*, (Ed.: P. J. Larkin), Elsevier, **2018**, pp. 75–84.

[74] A. Höpe in *Spectrophotometry*, (Eds.: T. A. Germer, J. C. Zwinkels, B. K. Tsai), Experimental Methods in the Physical Sciences, Academic Press, **2014**, pp. 179–219.

[75] F. C. Meunier, *React. Chem. Eng.* **2016**, *1*, 134–141.

[76] M. Bradley S., *Spectroscopy* **2015**, *30*, 42–46.

[77] N. M. Martin, P. Velin, M. Skoglundh, M. Bauer, P.-A. Carlsson, *Catal. Sci. Technol.* **2017**, *7*, 1086–1094.

[78] D. Bazin, D. Sayers, J. J. Rehr, C. Mottet, *The Journal of Physical Chemistry B* **1997**, *101*, 5332–5336.

[79] D. C. Bazin, D. A. Sayers, J. J. Rehr, *The Journal of Physical Chemistry B* **1997**, *101*, 11040–11050.

[80] A. Gayen, K. R. Priolkar, P. R. Sarode, V. Jayaram, M. S. Hegde, G. N. Subbanna, S. Emura, *Chemistry of Materials* **2004**, *16*, 2317–2328.

[81] S. Hosokawa, M. Taniguchi, K. Utani, H. Kanai, S. Imamura, *Applied Catalysis A: General* **2005**, *289*, 115–120.

[82] H. Hirata, K. Kishita, Y. Nagai, K. Dohmae, H. Shinjoh, S. Matsumoto, *Catalysis Today* **2011**, *164*, Innovations driven by catalysis - Selected papers from TOCAT6 / APCAT5, 467–473.

[83] V. Marchionni, M. A. Newton, A. Kambolis, S. K. Matam, A. Weidenkaff, D. Ferri, *Catalysis Today* **2014**, *229*, Advances in the use of X-rays for the characterization of functional catalytic materials, 80–87.

[84] Inorganic Crystal Structure Database, FIZ Karlsruhe, **2020**, `icsd.fiz-karlsruhe.de` (visited on 2021-03-03).

[85] A. Karelovic, P. Ruiz, *Applied Catalysis B: Environmental* **2012**, *113-114*, Natural Gas Conversion Symposium (NGCS 9) Special Issue, 237–249.

[86] I. A. Fisher, A. T. Bell, *Journal of Catalysis* **1996**, *162*, 54–65.

[87] A. Karelovic, P. Ruiz, *Journal of Catalysis* **2013**, *301*, 141–153.

[88] A. Kiennemann, R. Breault, J.-P. Hindermann, M. Laurin, *J. Chem. Soc., Faraday Trans. 1* **1987**, *83*, 2119–2128.

[89] G. N. Vayssilov, M. Mihaylov, P. S. Petkov, K. I. Hadjiivanov, K. M. Neyman, *The Journal of Physical Chemistry C* **2011**, *115*, 23435–23454.

[90] G. Krenn, I. Bako, R. Schennach, *The Journal of Chemical Physics* **2006**, *124*, 144703.

[91] C. Binet, M. Daturi, J.-C. Lavalley, *Catalysis Today* **1999**, *50*, 207–225.

[92] C. Li, Y. Sakata, T. Arai, K. Domen, K.-i. Maruya, T. Onishi, *J. Chem. Soc., Faraday Trans. 1* **1989**, *85*, 929–943.

[93] D. G. Araiza, A. Gómez-Cortés, G. Díaz, *Catal. Sci. Technol.* **2017**, *7*, 5224–5235.

[94] A. Beutler, E. Lundgren, R. Nyholm, J. Andersen, B. Setlik, D. Heskett, *Surface Science* **1998**, *396*, 117–136.

[95] D. Fernández-Torre, K. Kośmider, J. Carrasco, M. V. Ganduglia-Pirovano, R. Pérez, *The Journal of Physical Chemistry C* **2012**, *116*, 13584–13593.

[96] L. Luo, J. D. LaCoste, N. G. Khamidullina, E. Fox, D. D. Gang, R. Hernandez, H. Yan, *Surface Science* **2020**, *691*, 121486.

[97] J. Ye, C. Liu, D. Mei, Q. Ge, *ACS Catalysis* **2013**, *3*, 1296–1306.

[98] W. Barrett, J. Shen, Y. Hu, R. E. Hayes, R. W. J. Scott, N. Semagina, *ChemCatChem* **2020**, *12*, 944–952.

[99] M. V. d. Bossche, H. Grönbeck, *Journal of the American Chemical Society* **2015**, *137*, PMID: 26333148, 12035–12044.

[100] M. Digne, P. Sautet, P. Raybaud, P. Euzen, H. Toulhoat, *Journal of Catalysis* **2002**, *211*, 1–5.

[101] M. Digne, P. Sautet, P. Raybaud, P. Euzen, H. Toulhoat, *Journal of Catalysis* **2004**, *226*, 54–68.

[102] G. Busca, *Catalysis Today* **2014**, *226*, Acid-Base Catalysis Advanced Sciences and Spreading Applications to Solutions of Environmental, Resources and Energy Issues: ABC-7, 7th International Symposium on Acid-Base Catalysis, Tokyo, May 12-15, 2013, 2–13.

[103] X. Liu, R. E. Truitt, *Journal of the American Chemical Society* **1997**, *119*, 9856–9860.

[104] K. Helmut, P. Ratnasamy, *Catalysis Reviews* **1978**, *17*, 31–70.

[105] G. Busca, V. Lorenzelli, G. Ramis, R. J. Willey, *Langmuir* **1993**, *9*, 1492–1499.